

1

Title goes here

2

Bálint Balázs

3



4

Pázmány Péter Catholic University

5

Faculty of Information Technology

6



7

European Molecular Biology Laboratory

8

Supervisors: Lars Hufnagel, *PhD*, Balázs Rózsa, *MD, PhD*

9

A thesis submitted for the degree of

10

Doctor of Philosophy

11

2017

¹ Abstract

² Abstract in English.

¹ Tartalmi kivonat

² Absztrakt magyarul.

1 Contents

2	Abstract	iii
3	Tartalmi kivonat	v
4	List of Figures	xii
5	List of Tables	xiii
6	Introduction	1
7	1 Live imaging in three dimensions	3
8	1.1 Wide-field fluorescence microscopy	4
9	1.1.1 Fluorescent proteins	5
10	1.1.2 Wide-field image formation	5
11	1.1.3 Resolution of a wide-field microscope	7
12	1.2 Point scanning methods	10
13	1.2.1 Confocal laser scanning microscopy	12
14	1.2.2 Confocal-theta microscopy	14
15	1.3 Light-sheet microscopy	14
16	1.3.1 Optics of light-sheet microscopy	17
17	1.3.2 Static light-sheet illumination	17
18	1.3.3 Digitally scanned light-sheet illumination	20
19	1.4 Light-sheet microscopy for mouse imaging	22
20	1.4.1 Imaging pre-implantation	23
21	1.4.2 Imaging post-implantation development	24
22	1.4.3 Imaging adult mice	26
23	2 Dual Mouse-SPIM	29
24	2.1 Challenges in imaging mouse pre-implantation development	29
25	2.2 Microscope design principles	29
26	2.2.1 Light collection efficiency of an objective	29

1	2.2.2 Multi-view resolution	30
2	2.3 Optical layout	30
3	2.3.1 Illumination	32
4	2.3.2 Detection	32
5	2.4 Optical alignment	32
6	2.4.1 Alignment of illumination branches	32
7	2.4.2 Alignment of detection branches	35
8	2.5 Results	37
9	2.5.1 Characterizing illumination profile	38
10	2.5.2 Resolution and point spread function measurement	38
11	2.5.3 Stability of view switcher unit	39
12	3 Image processing for multi-view microscopy	41
13	3.1 Multi-view image fusion	42
14	3.1.1 Registration	42
15	3.1.2 Transformation	42
16	3.1.3 Image fusion	42
17	3.2 Image compression	42
18	3.2.1 Entropy coding	43
19	3.2.2 Transform coding	48
20	3.2.3 Differential pulse code modulation / LOCO-I?	52
21	3.3 Noise in light microscopy images	52
22	3.3.1 Photon shot noise	52
23	3.3.2 Camera noise	52
24	3.3.3 Variance stabilization	52
25	4 Real-time, GPU accelerated image processing pipeline	53
26	4.1 GPU architecture	53
27	4.2 Live fusion	53
28	4.2.1 MuVi-SPIM	53
29	4.2.2 Bead based registration	53
30	4.3 B ³ D image compression	53
31	4.3.1 Data sizes in microscopy	53
32	4.3.2 Lossless compression performance	53
33	4.3.3 Benchmarking	53
34	4.4 Noise dependent lossy compression	53
35	4.5 Methods	53

1	5 Discussion	59
2	5.1 New scientific results	59
3	Acknowledgements	61
4	Appendix A: Bill of materials	63
5	References	65

CONTENTS

¹ List of Figures

2	1.1	Tradeoffs in fluorescence microscopy for live imaging	4
3	1.2	Excitation and emission spectrum of enhanced green fluorescent protein (EGFP)	5
4	1.3	Wide-field fluorescence microscope	6
5	1.4	Axial cross section of the PSF and OTF of a wide-field microscope	8
6	1.5	Airy pattern	9
7	1.6	Resolution of a wide-field microscope	11
8	1.7	Basic optical components of a confocal laser scanning and confocal-theta microscope	12
9	1.8	Axial cross section of the PSF and OTF of a confocal laser scanning mi- croscope	13
10	1.9	Basic concept of single-plane illumination microscopy	15
11	1.10	Different optical arrangements for light-sheet microscopy	16
12	1.11	Basic optical components of a SPIM	18
13	1.12	Light-sheet dimensions	19
14	1.13	DSLM illumination	21
15	1.14	Inverted light-sheet microscope for multiple early mouse embryo imaging.	24
16	1.15	Imaging mouse post-implantation development	25
17	1.16	Imaging adult mouse brain with light-sheet microscopy.	27
18	2.1	Light collection efficiency of an objective	31
19	2.2	Axial cross section of the PSF and OTF of a multi-view single plane illumination microscope	31
20	2.3	Simplified schematics for illumination	32
21	2.4	Dual Mouse SPIM optical layout	33
22	2.5	Illumination branch splitting block	34
23	2.6	Detection branch merging unit	35
24	2.7	Front view of the Dual Mouse-SPIM	37
25	2.8	Illumination beam profile	38

LIST OF FIGURES

1	2.9 Schematics for the Gibson-Lanni model	39
2	2.10 Simulated and measured PSF of Dual Mouse-SPIM	40
3	3.1 Building the binary Huffman tree	45
4	3.2 Arithmetic coding scheme in practice with the alphabet from Table 3.4 on the sequence a_1, a_2, a_3	47
5	3.3 Basis functions of the 8×8 2D DCT, computed as the outer product of the 1D basis vectors.	49
6	3.4 Multi-resolution wavelet decomposition, using the Haar wavelets as an example	51
7		
8	4.1 Experiment sizes and data rate of different imaging modalities.	54
9	4.2 Lossless compression performance	55
10	4.3 Within noise level compression performance.	57
11		
12		

¹ List of Tables

2	3.1 Examples of a random binary code (#1) and a prefix-free binary code (#2)	44
3	3.2 Huffman code table	45
4	3.3 Huffman code table	46
5	3.4 Example alphabet for arithmetic coding	47
6	4.1 Data sizes in microscopy	54
7	4.2 Lossless compression performance	55
8	4.3 Datasets used for benchmarking compression performance	56

LIST OF TABLES

¹ Introduction

² Coming soon.

INTRODUCTION

¹ Chapter 1

² Live imaging in three dimensions

³ Unraveling the secrets of mammalian development has been a long standing challenge
⁴ for developmental biologists and medical professionals alike. This phase of early life is
⁵ an incredibly complex and dynamic process spanning through large scales in space and
⁶ time. Subcellular processes at the nanoscale are happening in the range of milliseconds
⁷ or faster, while whole embryo reorganizations and tissue migration events take place over
⁸ the course of hours [1]. Resolving these processes presents a true challenge, since to also
⁹ understand the underlying mechanisms molecular specificity is just as crucial as high
¹⁰ spatial and temporal resolution.

¹¹ Light microscopy is one of the oldest methods that is still widely used today to
¹² investigate the inner workings of microscopic life. A particularly important branch is
¹³ fluorescence microscopy [2], that relies on using fluorescent labels to mark specific regions
¹⁴ inside the specimens. Light-sheet microscopy is a relatively new addition to the arsenal of
¹⁵ tools that comprise light microscopy methods, and is especially suitable for live imaging
¹⁶ of embryonic samples over extended periods of time [3, 4]. It is also easily adapted to
¹⁷ the sample, allowing to image a large variety of specimens, from entire organs, such as
¹⁸ cleared mouse brains [5], to the subcellular processes occurring inside cultured cells [6].

¹⁹ In an ideal setting, the ultimate microscope would be able to record a continuos,
²⁰ 3D, and multicolor dataset of any biological process of interest with the highest possible
²¹ resolution. Unfortunately this is not possible; due to several limitations in physics and
²² biology, a compromise is necessary. The diffractive nature of light, the lifetime of fluo-
²³ rescent probes and the photosensitivity of biological specimens all require microscopy to
²⁴ be able to adapt to answer the question at hand. In order to acquire useful data one has
²⁵ to choose a tradeoff between spatial and temporal resolution, and signal contrast, while
²⁶ making sure the biology is not affected by the imaging process itself (Fig. 1.1) [7].

1. LIVE IMAGING IN THREE DIMENSIONS

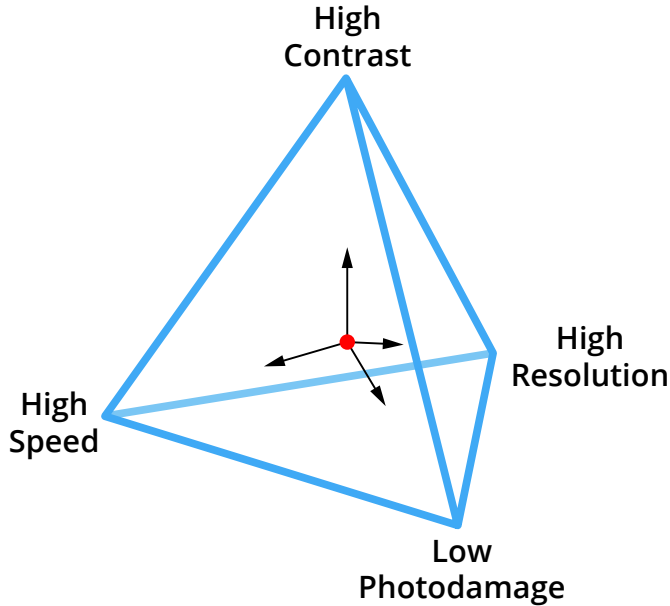


Figure 1.1: Tradeoffs in fluorescence microscopy for live imaging. Also called the “pyramid of frustration”. When optimizing the imaging conditions (red dot), a tradeoff has to be made between resolution, contrast, and imaging speed, while avoiding photodamage. One can only be improved at the expense of the others due to the limited photon budget of the fluorescent molecules. Adapted from [7].

¹ 1.1 Wide-field fluorescence microscopy

² Fluorescence microscopy [2, 8], as a subset of light microscopy is one of the few methods
³ that allow subcellular imaging of live specimens. The first use of the term fluorescence is
⁴ credited to George Gabriel Stokes [9], and it refers to the phenomenon when a molecule
⁵ emits light after absorbing light or other electromagnetic radiation. As the name of the
⁶ technique suggests, this method collects fluorescent light from the specimens which has
⁷ numerous advantages, but also some drawbacks. Since biological tissue is usually not
⁸ fluorescent, except for some autofluorescence at shorter wavelengths, fluorescent dyes or
⁹ proteins have to be introduced to the system in order to be able to collect the necessary
¹⁰ information. The advantage of this is that the signal of the labeled structures will be of
¹¹ very high ratio compared to the background.

¹² A fluorescent molecule is capable of absorbing photons in a given range (excitation
¹³ spectrum) and temporarily store its energy by having an electron in a higher energy
¹⁴ orbital, *i.e.* in an excited state. This excited state, however is not stable, and the electron
¹⁵ quickly jumps back to the ground state while emitting a photon with equal energy to the
¹⁶ energy difference between the excited and ground states. The energy of the absorbed and
¹⁷ emitted photons are not the same, as energy loss occurs due to internal relaxation events,
¹⁸ and the emitted photon has lower energy than the absorbed photon. This phenomenon
¹⁹ is called the Stokes shift, or red shift, and can be exploited in microscopy to drastically
²⁰ increase the signal to noise ratio by filtering out the illumination light (Fig. 1.2).

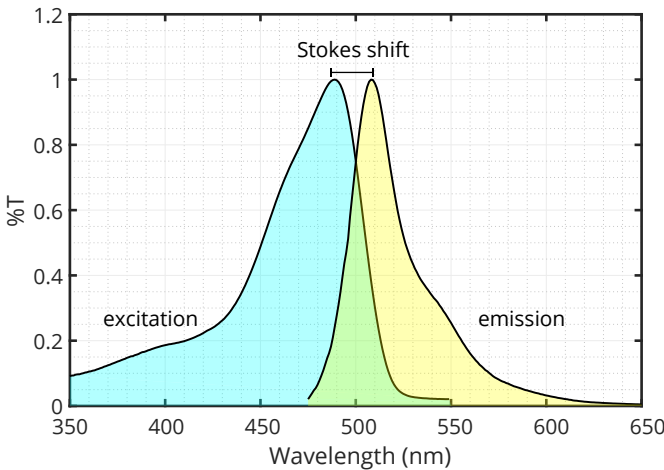


Figure 1.2: Excitation and emission spectrum of enhanced green fluorescent protein (EGFP). Excitation spectrum in blue, emission spectrum in yellow. The separation between the two spectra is due to the Stokes shift, which is 19 nm for EGFP. Emitted and excitation light can be separated by a long-pass filter at 500 nm. Data from [10].

¹ 1.1.1 Fluorescent proteins

² Traditionally synthetic fluorescent dyes were used to label certain structures in the specimens.
³ Some of these directly bind to their target, and others can be used when conjugated
⁴ to an antibody specific to the structure of interest. The drawback of these methods is
⁵ that the fluorescent label has to be added to the sample from an external source, and, in
⁶ many cases, this also necessitates sample preparation techniques incompatible with live
⁷ imaging, such as fixation [11].

⁸ The discovery of fluorescent proteins have revolutionized fluorescence microscopy.
⁹ Since these molecules are proteins, they can be produced directly by the organism if
¹⁰ the proper genetic modifications are performed. Even though this was a hurdle at the
¹¹ time of discovering the green fluorescent protein (GFP) [12], the first of its kind, genetic
¹² engineering techniques evolved since then [13], and not only has it been successfully
¹³ integrated in the genome of nematodes [14], zebrafish [15], and mice [16], but many
¹⁴ variants have been also engineered by introducing mutations to increase fluorescence
¹⁵ intensity, and to change the fluorescence spectrum to allow multicolor imaging [16–19].
¹⁶ The usefulness and impact of these proteins are so profound, that in 2008 the Nobel
¹⁷ Prize in chemistry was awarded to Osamu Shimomura, Martin Chalfie, and Roger Tsien
¹⁸ “for the discovery and development of the green fluorescent protein, GFP” [20].

¹⁹ 1.1.2 Wide-field image formation

²⁰ By imaging fluorescently labelled specimens, a wide-field fluorescence microscope has the
²¹ capability of discriminating illumination light from fluorescent light due to the Stokes
²² shift described in the previous section. The microscope’s operating principle is depicted

1. LIVE IMAGING IN THREE DIMENSIONS

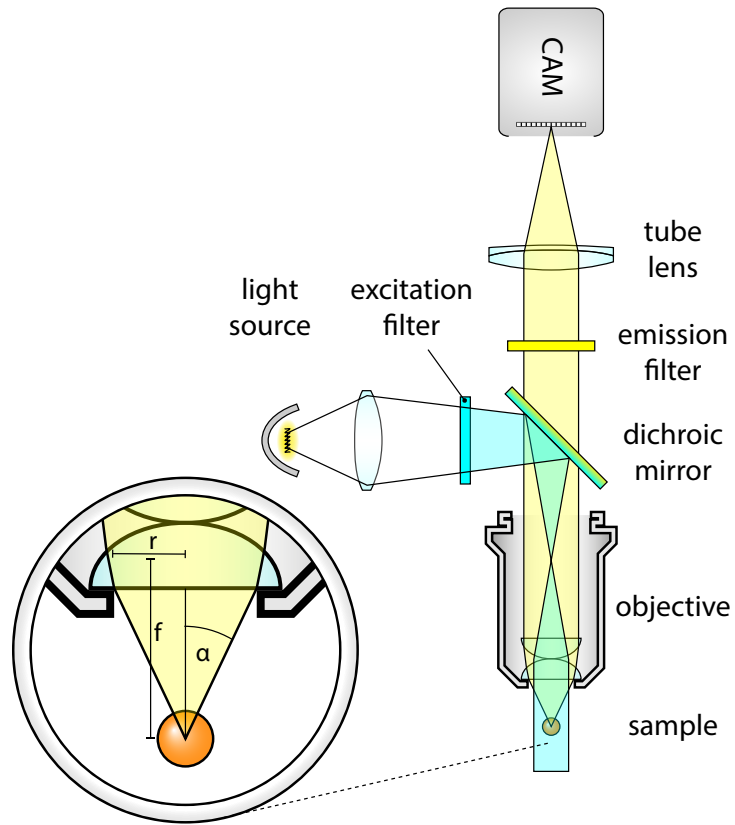


Figure 1.3: Wide-field fluorescence microscope. (a) The light source is focused on the back focal plane of the objective to provide an even illumination to the sample. Emitted photons are collected by the objective, and are separated from the illumination light by a dichroic mirror. (b) , α

1 in Figure 1.3.

2 A light source, typically a mercury lamp is focused on the back focal plane of the
3 objective to create even illumination at the sample. Before entering the objective, the
4 light is filtered, so only those wavelengths that correspond to the excitation properties
5 of the observed fluorophores are transmitted. Since the same objective is used for both
6 illumination and detection, a dichroic mirror is utilized to decouple the illumination
7 and detection paths. The emitted light is filtered again to make sure any reflected and
8 scattered light from the illumination source is blocked to increase signal to noise ratio.

9 Finally, the light is focused by a tube lens to create a magnified image in the cam-
10 era sensor. This type of imaging is called infinity corrected optics, since the back focal
11 point of the objective is in “infinity”, meaning that the light exiting the back aperture is
12 parallel. This is achieved by placing the sample exactly at the focal point of the objec-
13 tive. Infinity corrected optics has the advantage that it allows placing various additional
14 optical elements in the infinity space (*i.e.* the space between the objective and the tube
15 lens) without affecting the image quality. In this example such elements are the dichroic
16 mirror and the emission filter.

¹ The combination of the objective and tube lens together will determine the magnification of the system, it will be the ratio of the focal lengths of these lenses:

$$M = \frac{f_{TL}}{f_{OBJ}}. \quad (1.1)$$

³ The final field of view of the microscope will depend on the magnification, and also on
⁴ the size of the imaging sensor:

$$FOV = \frac{A}{M}, \quad (1.2)$$

⁵ where A is the area of the sensor.

⁶ Apart from magnification, the most important property of the objective is the half-angle of the light acceptance cone, α . This not only determines the amount of collected
⁷ light, but also the achievable resolution of the system (see next section). This angle
⁸ depends on the size of the lens relative to its focal length. In other words depends on
⁹ the aperture of the lens, which is why the expression *numerical aperture* (NA) is more
¹⁰ commonly used to express this property of the objective:
¹¹

$$NA = n \cdot \sin \alpha. \quad (1.3)$$

¹² For small α angles, the following approximation holds true: $\sin \alpha \approx \tan \alpha \approx \alpha$. Thus,
¹³ the numerical aperture can also be expressed as a ratio of the radius of the lens and the
¹⁴ focal length:

$$NA \approx n \frac{r}{f}, \quad \text{when } \alpha \ll 1. \quad (1.4)$$

¹⁵ 1.1.3 Resolution of a wide-field microscope

¹⁶ The resolution of an optical systems is defined by the size of the smallest distinguishable
¹⁷ feature on the image. Practically this means the minimum distance between two point-like objects so that the two objects can still be resolved. This mainly depends on two
¹⁸ factors: the NA of the objective, and the pixel size of the imaging sensor.
¹⁹

²⁰ Even if the imaging sensor would have infinitely fine resolution, it is not possible to
²¹ reach arbitrary high resolutions due to the wave nature of light and diffraction effects
²² that occur at the aperture of the objective. This means that depending on the wavelength
²³ of the light, any point source will have a finite size on the image, it will be spread out,
²⁴ that will limit the resolution. The shape of this image is called the *point spread function*,
²⁵ or PSF (Fig. 1.4), as this function describes the behavior of the optical system when
²⁶ imaging a point like source. This property of lenses was already discovered by Abbe in
²⁷ 1873 [21], when he constructed his famous formula for resolution:

$$\delta = \frac{\lambda}{2 \cdot NA}. \quad (1.5)$$

1. LIVE IMAGING IN THREE DIMENSIONS

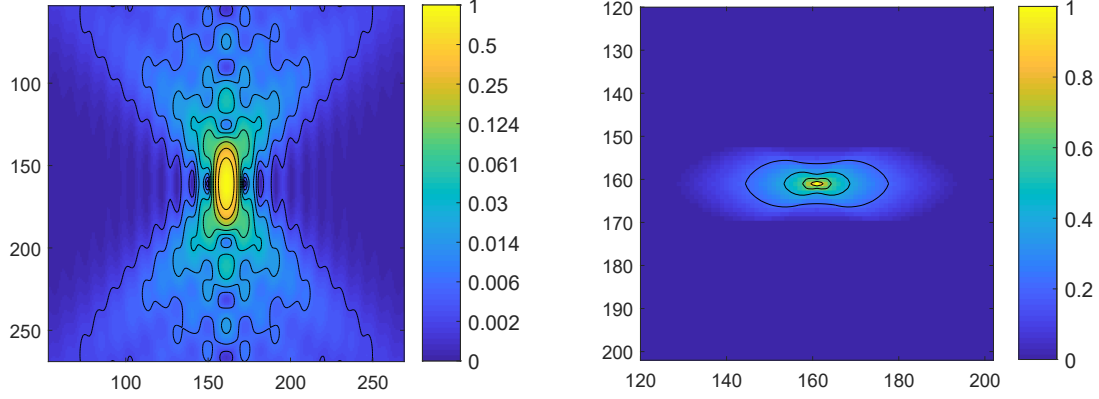


Figure 1.4: Axial cross section of the PSF and OTF of a wide-field microscope. Simulated PSF and OTF for a wide-field microscope with a water immersion objective ($n = 1.33$). $NA = 1.1$, $\lambda = 510\text{ nm}$

- ¹ where d is the smallest distance between two distinguishable features.
- ² Another representation of the optical performance, is the *optical transfer function*,
- ³ or OTF (Fig. 1.4), which is the Fourier transform of the PSF:

$$\text{OTF} = F(\text{PSF}). \quad (1.6)$$

- ⁴ As this function operates in the frequency space, it describes how the different frequencies
- ⁵ are affected by the system. The resolution can also be defined as the support of the OTF,
- ⁶ since this describes the highest frequency that is still transmitted through the optical
- ⁷ system. Any pattern with higher frequency will be lost, thus beyond the resolution limit.
- ⁸ For circularly symmetric PSFs, the OTF will be real valued, however if this is not the
- ⁹ case, the Fourier transform also introduces complex components.

¹⁰ Abbe's formula can be derived from the scalar theory of diffraction using a paraxial

¹¹ approximation (Fraunhofer diffraction, [22]) that describes the intensity of the electric

¹² field in the focus of a lens [23]:

$$H(u, v) = C_0 \left| \int_0^1 J_0(vr) e^{-i\frac{1}{2} \cdot ur^2} r dr \right|^2, \quad (1.7)$$

¹³ where C_0 is a normalization constant, and J_0 is the zero order Bessel function of the first

¹⁴ kind. Furthermore, instead of the commonly used Cartesian coordinates x , y and z , the

¹⁵ following optical coordinates are defined:

$$v = \frac{2\pi nr}{\lambda_0} \sin \alpha, \quad u = \frac{8\pi nz}{\lambda_0} \sin^2 \frac{\alpha}{2} \quad (1.8)$$

¹⁶ where $r = \sqrt{x^2 + y^2}$ is the distance from the optical axis, and α is the light collection

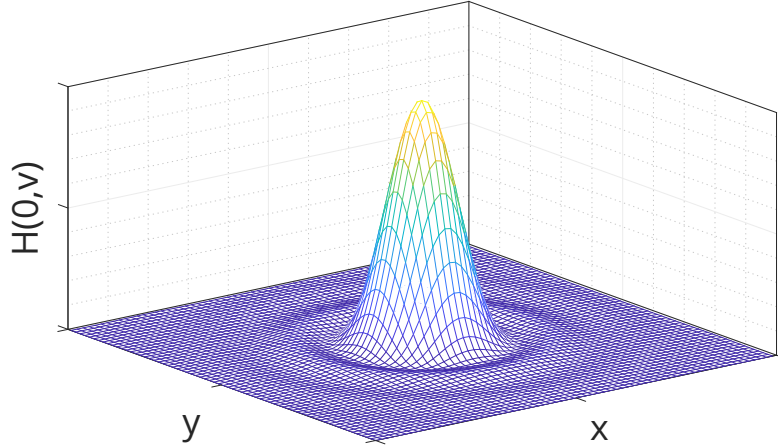


Figure 1.5: Airy pattern. Airy pattern calculated in Matlab based on Eq. 1.9

1 angle as shown on Fig. 1.3.

2 To determine the lateral resolution of the system, let's substitute $u = 0$ as the axial
3 optical coordinate, and evaluate Eq. 1.7 which will give the intensity distribution inn the
4 focal plane:

$$H(0, v) = C_0 \left| \int_0^1 J_0(vr) r dr \right|^2 = \left(2 \frac{J_1(v)}{v} \right)^2, \quad (1.9)$$

5

6 where J_1 is the first order Bessel function of the first kind. This equation describes
7 the famous Airy pattern (Fig. 1.5) which will be the shape of the PSF in the focal plane.
8 The width of this pattern is the resolution, and although there are multiple definitions
9 for this, the most commonly accepted is the Rayleigh criterion [22, 24] which defines the
10 resolution as the distance between the central peak and the first local minimum. As this
11 lies at $v = 3.88$, the resolution can be expressed by substituting this value to Eq. 1.8 and
12 calculating the real distance (r):

$$\delta_{xy} = \frac{3.83}{2\pi} \frac{\lambda_0}{n \cdot \sin \alpha} \approx 0.61 \frac{\lambda_0}{NA}, \quad (1.10)$$

13 which is equivalent to Abbe's original formula (Eq. 1.5). The only difference is the scaling
14 factor which is due to the slightly different interpretations of width of the Airy disk as
15 mentioned earlier.

16 Similarly, to calculate the intensity distribution along the axial direction, let's sub-
17 stitute $v = 0$ to Eq. 1.7:

$$H(u, 0) = C_0 \left(\frac{\sin \frac{u}{4}}{\frac{u}{4}} \right)^2. \quad (1.11)$$

18 For this expression the first minimum lies at $u = 4\pi$. Converting back to Cartesian

1. LIVE IMAGING IN THREE DIMENSIONS

¹ coordinates, the axial resolution can be expressed as:

$$\delta_z = \frac{2n\lambda_0}{NA^2}. \quad (1.12)$$

² So far we only considered a single, point-like emitter. As the intensity function de-
³ scribes how an optical system “spreads out” the image of a point, it is also called the
⁴ Point Spread Function (PSF, Fig. 1.4). In a more realistic scenario, however the emitters
⁵ are neither point-like, nor single. Effectively, however, for every emitter the PSF would
⁶ be imaged on the sensor, and this creates the final image. In mathematical terms, this can
⁷ be expressed as a convolution operation between the underlying fluorophore distribution
⁸ of the object (O) and the PSF (H):

$$I(u, v) = O(u, v) * H(u, v). \quad (1.13)$$

⁹ The effective result of this kind of diffraction limited image formation is a blurred
¹⁰ image with a finite resolution of δ_{xy} in the lateral direction, and δ_z in the axial direction.

¹¹ The PSF is further affected by the illumination pattern as well. Since the number of
¹² emitted fluorescent photons are roughly proportional to the illumination intensity, if the
¹³ illumination has any structure at the order of the detection resolution, it will have an
¹⁴ effect on the overall PSF of the system, which can be expressed as:

$$H_{sys} = H_{ill} \cdot H_{det}, \quad (1.14)$$

¹⁵ where H_{ill} is the point spread function of the illumination, and H_{det} is the point spread
¹⁶ function of the detection.

¹⁷ 1.2 Point scanning methods

¹⁸ In most cases, a wide-field microscope is used to image a section of a tissue, thus axial
¹⁹ resolution is not a concern. Imaging live specimens, however is not so straightforward,
²⁰ as these samples are usually much thicker than a typical section. For these samples 3-
²¹ dimensional (3D) imaging is highly beneficial, which necessitates some kind of optical
²² sectioning technique to be able to discriminate the features at different depths.

²³ Due to the design of the wide-field microscope, any photons emitted from outside the
²⁴ focal plane will also be detected by the sensor, however as these are not originating from
²⁵ the focus, only a blur will be visible. This blur potentially degrades image quality and
²⁶ signal-to-noise ratio to such extent that makes imaging thick sample very difficult if not
²⁷ impossible in a wide-field microscope.

²⁸ Evaluating Equations 1.10 and 1.12 for a range of possible numerical apertures reveals

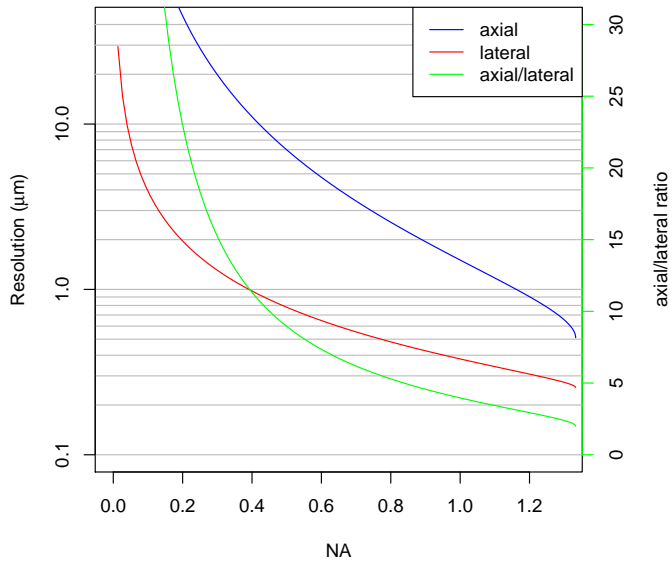


Figure 1.6: Resolution of a wide-field microscope. Axial (blue) and lateral (red) resolutions of a wide-field microscope are shown with respect to the numerical aperture (NA). Resolutions are calculated with $\lambda = 510\text{nm}$, the emission maximum of GFP and $n = 1.33$, the refractive index of water, for water dipping objectives.

1 the significant differences in lateral and axial resolution for any objective (Fig. 1.6).
 2 Especially for low NAs, this can be significant, a factor of ~ 20 difference. For higher
 3 (>0.8) NAs the axial resolution increases faster than the lateral, however they will only
 4 be equal when $\alpha = 180^\circ$. This means that isotropic resolution with a single lens is only
 5 possible if the lens is collecting all light emitting from the sample, which seems hardly
 6 possible, and would be highly impractical. For commonly used high NA objectives the
 7 lateral to axial ratio will still be around 3–6.

8 Instead of using a single lens to achieve isotropic resolution, it's more practical to
 9 image the sample from multiple directions to complement the missing information from
 10 different views. When rotating the sample 90° for example, the lateral direction of the
 11 second view will correspond to the axial direction of the first view. If rotation is not
 12 possible, using multiple objectives can also achieve similar result, such as in the case of
 13 Multi-Imaging Axis Microscopy (MIAM) [25, 26]. This microscope consisted of 4 identical
 14 objectives arranged in a tetrahedral fashion to collect as much light as possible from mul-
 15 tiple directions, and provide isotropic 3D resolution, albeit at the expense of extremely
 16 difficult sample handling, since the sample was completely surrounded by objectives from
 17 all directions.

1. LIVE IMAGING IN THREE DIMENSIONS

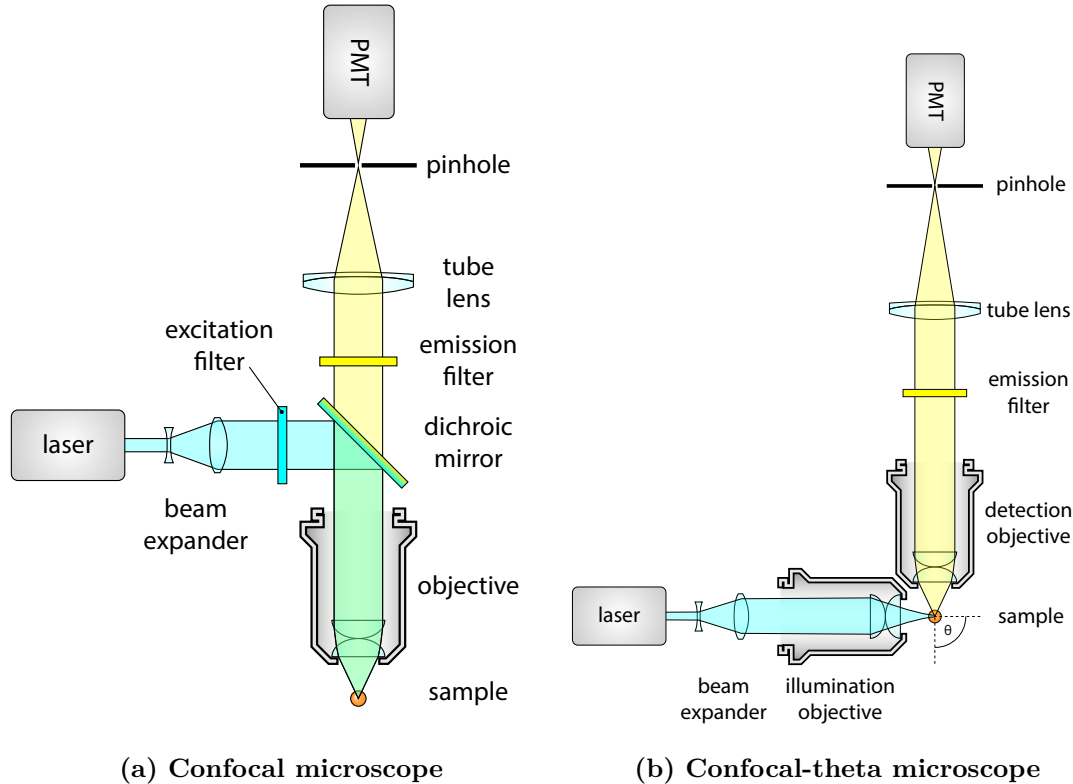


Figure 1.7: Basic optical components of a confocal laser scanning and confocal-theta microscope. Both type of microscopes use confocal images detection, which means that a pinhole is used to exclude light coming from out of focus points. Light intensity is measured by a photomultiplier for every voxel in the region of interest. The final image is generated on a computer using the positions and recorded intensity values. A regular confocal microscope (1.7a) uses the same objective for illumination and detection, while a confocal-theta microscope (1.7b) uses a second objective that is rotated by ϑ around the focus. In this case, $\vartheta = 90^\circ$.

¹ 1.2.1 Confocal laser scanning microscopy

² Confocal laser scanning microscopy (CLSM) [27, 28] addresses most of the problems
³ of wide-field microscopy we mentioned in the previous section. It is capable of optical
⁴ sectioning by rejecting out of focus light, which makes it a true 3D imaging technique.
⁵ Furthermore, the light rejection also massively reduces out of focus background, and
⁶ increases contrast.

⁷ This is achieved by two significant modifications compared to the wide-field optical
⁸ path. To be able to reject the out of focus light, an adjustable pinhole is placed at the focus
⁹ of the tube lens. Light rays originating from the focal point will meet at this position,
¹⁰ and are able to pass through the pinhole, however out-of-focus light will converge either
¹¹ before or after the aperture, and thus the aperture blocks these rays. To maximize the
¹² fluorescence readout efficiency for the single focal point, a photomultiplier tube is used
¹³ instead of an area sensor (Fig. 1.7a).

¹⁴ To maximize the signal from the focal point, the illumination light is also focused

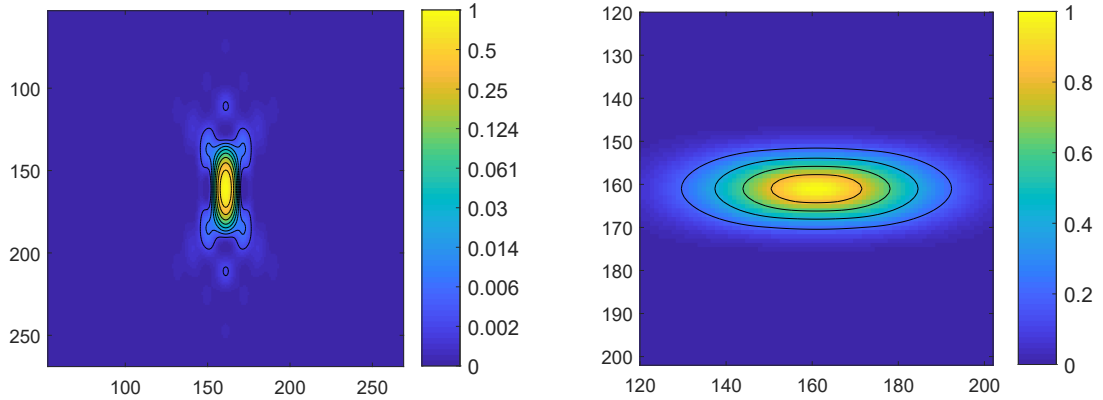


Figure 1.8: Axial cross section of the PSF and OTF of a confocal laser scanning microscope. Simulated PSF and OTF for a laser scanning confocal microscope with a water immersion objective ($n = 1.33$). $NA = 1.1$, $\lambda = 510\text{ nm}$

1 here by coupling an expanded laser beam through the back aperture of the objective.
 2 This not only increases illumination efficiency (since other, not detected points are not
 3 illuminated), but has the added benefit of increasing the resolution as well. This is due to
 4 the combined effect of illumination and detection PSFs as described in Eq. 1.14 (Fig. 1.8).
 5 For Gaussian-like PSFs, the final resolution (along a single direction) can be calculated
 6 in the following way:

$$\frac{1}{\delta_{sys}^2} = \frac{1}{\delta_{ill}^2} + \frac{1}{\delta_{det}^2}, \quad (1.15)$$

7 where δ_{ill} and δ_{det} are the resolutions for the illumination and detection, respectively.
 8 Since the same objective is used for both illumination and detection, and the difference
 9 in wavelength is almost negligible, $\delta_{ill} = \delta_{det} = \delta$, the final system resolution will be:

$$\delta_{sys} = \frac{1}{\sqrt{2}}\delta. \quad (1.16)$$

10 This means that the distinguishable features in a confocal microscope are ~ 0.7 times
 11 smaller than in a wide-field microscope using the same objective.

12 Because of the different detection method in a confocal microscope, direct image
 13 formation on an area sensor is not possible, since at any given time, only a single point is
 14 interrogated in the sample. Instead, it's necessary to move the illumination and detection
 15 point in synchrony (or in a simpler, albeit slower solution, to move the sample) to scan
 16 the entire field of view. The image can be later computationally reconstructed by a
 17 computer program that records the fluorescence intensity of every point of the field of
 18 view, and displays these values as a raster image.

1. LIVE IMAGING IN THREE DIMENSIONS

1.2.2 Confocal-theta microscopy

Although confocal microscopy already has 3D capabilities, its axial resolution is still limited compared to the lateral, since it uses only one objective. An alternative realization of the confocal microscope, the confocal theta microscope [29] introduces a second objective to the system, that is used to illuminate the sample (Fig. 1.7b). Since this decouples the illumination and detection, using a filter cube is no longer necessary. The second objective is rotated by θ around the focus, this is where the name of this setup originates from.

As in the case of standard confocal microscopy, the system PSF is improved by the illumination pattern. Here, however, the axial direction of the detection coincides with the lateral direction of the illumination, which results in a dramatic improvement of axial resolution compared to standard confocal microscopy. Lateral resolution will also be increased, but by a smaller extent, resulting in an almost isotropic PSF, and equal axial and lateral resolutions (Fig. ??).

Although this is a big improvement to confocal microscopy in terms of resolution, this technique did not reach a widespread adoption as it complicates sample handling, while still suffering from two big drawbacks of confocal microscopy techniques that limits its live imaging capabilities.

Imaging live specimens for an extended period of time with confocal microscopy although possible [30, 31], is not ideal. For each voxel imaged, a large portion of the specimen has to be illuminated, which results in a very high dose of radiation on the samples. This can be as much as 30–100 times larger, than the dose used for the actual imaging [32]. Illumination with high power of laser for an extended time frame can result in bleaching the fluorophores, which in turn will lower the signal at later times. Furthermore, any absorbed photon has the possibility to disrupt the chemical bonds inside the specimen, which can lead to phototoxic effects. Moreover, the usage of the pinhole although increases resolution, also decreases the detectable signal intensity, thus has a negative impact on image contrast [33].

1.3 Light-sheet microscopy

A selective-plane illumination microscope (SPIM) uses a light-sheet to illuminate only a thin section of the sample (Fig. 1.9). This illumination plane is perpendicular to the imaging axis of the detection objective and coincides with the focal plane. This way, only the section in focus will be illuminated, thus providing much better signal to noise ratio. In case of conventional wide-field fluorescence microscopy, where the whole specimen is illuminated, light scattering from different regions contributes to a significant background noise. With selective-plane illumination, this problem is intrinsically solved, and it also

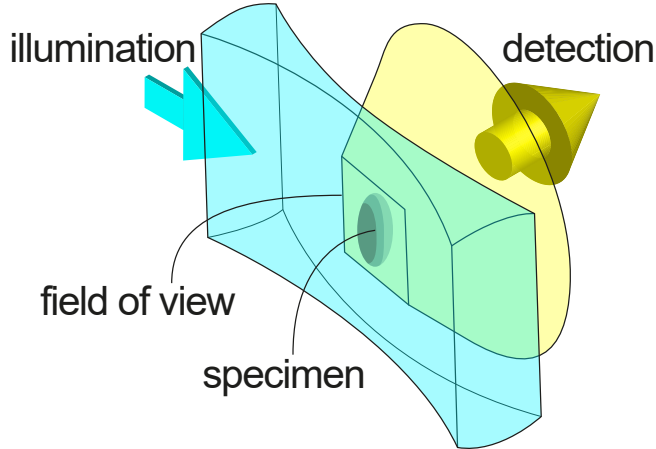


Figure 1.9: Basic concept of single-plane illumination microscopy. The sample is illuminated from the side by laser light shaped to a light-sheet (blue). This illuminates the focal plane of the detection lens, that collects light in a wide-field mode (yellow). The image is recorded, and the sample is translated through the light-sheet to acquire an entire 3D stack.

provides a true sectioning capability. This makes SPIM especially suitable for 3D imaging.
 The main principle behind single plane illumination microscopy, that is illuminating the sample from the side by a very thin light-sheet, dates back to the early 20th century, when Siedentopf and Zsigmondy first described the ultramicroscope [34]. This microscope used sunlight as an illumination source, that was guided through a precision slit to generate a thin light-sheet. This allowed Zsigmondy to visualize gold nanoparticles floating in and out of the light-sheet. Since these particles are much smaller than the wavelength of the light, the device was called an ultramicroscope. His studies with colloids, and the development of the ultramicroscope led Zsigmondy to win the Nobel Prize in 1925.

After Zsigmondy, this method was forgotten until rediscovered in the 1990s, when Voie *et al.* constructed their Orthogonal-plane Fluorescent Optical Sectioning (OPFOS) microscope [35]. They used it to image a fixed, optically cleared and fluorescently labelled guinea pig cochlea. In order to acquire a 3D dataset, the sample was illuminated from the side with a light-sheet generated by a cylindrical lens, then rotated around the center axis to obtain multiple views. Although they only reached a lateral resolution around 10 µm and axial resolution of 26 µm, this method allowed them to generate a 3D reconstruction of the cochlea [36].

Later, in 2002, Fuchs *et al.* developed Thin Light-Sheet Microscopy (TLSM) [37] and used this technique to investigate the microbial life in seawater samples without disturbing their natural environment (by e.g. placing them on a coverslip). Their light-sheet was similar to the one utilized in OPFOS, being 23 µm thin, and providing a 1 mm × 1 mm field of view.

Despite these early efforts, the method did not gain larger momentum. The real

1. LIVE IMAGING IN THREE DIMENSIONS

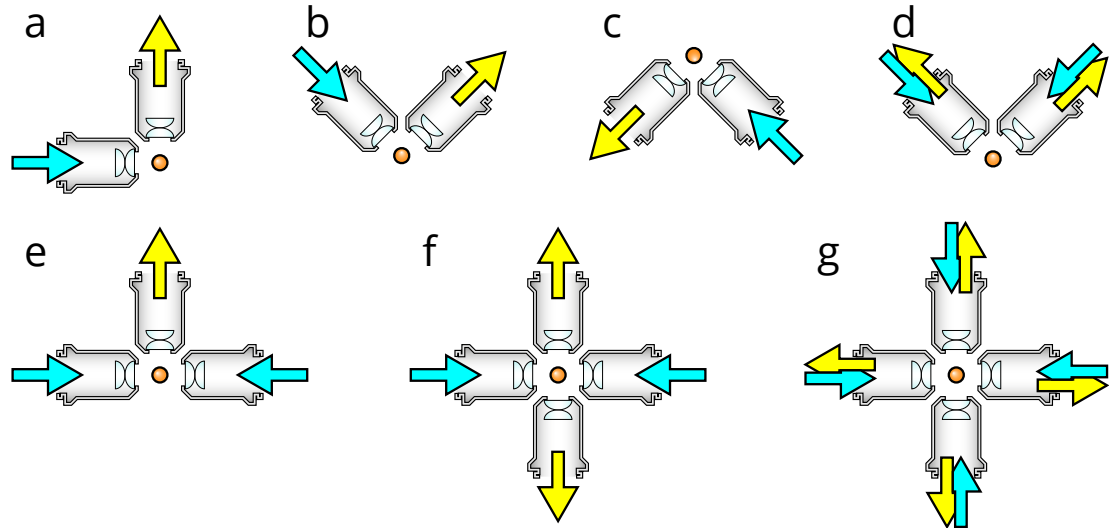


Figure 1.10: Different optical arrangements for light-sheet microscopy. (a) Original SPIM design with a single lens for detection and illumination. [38] (b) Upright SPIM to allow for easier sample mounting such as using a petri dish (iSPIM, [39, 40, J1]). (c) Inverted SPIM, where the objectives are below the sample, which is held by a thin foil [J2]. (d) Dual-view version of the upright configuration, where both objective can be used for illumination and detection (disPIM, [41]). (e) Multidirectional-SPIM (mSPIM) for even illumination of the sample with two objectives for illumination [42]. (f) Multi-view SPIM with two illumination and detection objectives for *in toto* imaging of whole embryos (MuVi-SPIM [3], SimView [4], Four-lens SPIM [43]). (g) A combination of (d) and (f), using four identical objectives, where both can illuminate and detect in a sequential manner, to achieve isotropic resolution without sample rotation (IsoView [44]).

1 breakthrough in light-sheet imaging happened at EMBL in 2004, where Huisken *et al.* [38]
 2 combined the advantages of endogenous fluorescent proteins and the optical sectioning
 3 capability of light-sheet illumination to image Medaka fish embryos, and the complete
 4 embryonic development of a *Drosophila melanogaster* embryo. They called this Selective-
 5 Plane Illumination Microscopy (SPIM), and it quickly became popular to investigate
 6 developmental biological questions.

7 Since then, light-sheet based imaging has gained more and more popularity, as it can
 8 be adapted and applied to a wide variety of problems. Although sample mounting can
 9 be challenging because of the objective arrangement, this can also be an advantage, since
 10 new microscopes can be designed with the sample in mind [45, J3] (Fig. 1.10). This made
 11 it possible to adapt the technique for numerous other specimens, such as zebrafish larvae
 12 [46], *C. elegans* embryos [40], mouse brain [5], and even mouse embryos [J2, 47, 48].

13 As many of these specimens require very different conditions and mounting tech-
 14 niques, these microscopes have been adapted to best accommodate them. An upright
 15 objective arrangement for example (Fig 1.10b) allows imaging samples on a coverslip,
 16 while its inverted version is well suited for mouse embryos, where a foil is separating them
 17 from the immersion medium (Fig. 1.10c). A modified version of the upright arrangement
 18 allows for multi-view imaging using both objectives for illumination and a

1 sequential manner (Fig. 1.10d) [41].

2 For larger samples, to achieve a more even illumination, two objectives can be used
3 from opposing directions to generate two light-sheets (Fig. 1.10e) [42]. This arrangement
4 can further be complemented by a second detection objective, to achieve parallelized
5 multi-view imaging (Fig. 1.10f) [3, 4, 43]. For ultimate speed, 4 identical objectives can
6 be used to achieve almost instantaneous views from 4 different directions by using all
7 objectives for illumination and detection (Fig 1.10g) [44].

8 Furthermore, because of the wide-field detection scheme it is possible to combine
9 SPIM with many superresolution techniques, such as single molecule localization [49],
10 STED [50], RESOLFT [J1], or structured illumination [6, 51, 52].

11 1.3.1 Optics of light-sheet microscopy

12 Since illumination and detection for light-sheet microscopy are decoupled, two indepen-
13 dent optical paths are implemented.

14 The detection unit of a SPIM is basically equivalent to a detection unit of a wide-
15 field microscope, without a dichroic mirror (Fig. 1.11). Most important components are
16 the objective together with the tube lens, filter wheel, and a sensor, typically a CCD or
17 sCMOS camera.

18 One of the most important aspects that determine the resolution of the microscope is
19 the detection objective. Since imaging biological specimens usually requires a water-based
20 solution, the objectives also need to be directly submerged in the medium to minimize
21 spherical aberrations. Since the refraction index of water ($n = 1.33$) is greater than the
22 refraction index of air, these objectives tend to have a higher NA, which results in higher
23 resolution. The final resolution, however, also depends on the pixel size of the sensor
24 which determines the spatial sampling rate of the image.

25 Although image quality and resolution greatly depends on the detection optics, the
26 real strength of light-sheet microscopy, the inherent optical sectioning is due to the
27 specially designed illumination pattern, that confines light to the vicinity of the detection
28 focal plane.

29 There are two most commonly used options to generate a light-sheet: either by using
30 a cylindrical lens, to illuminate the whole field of view with a static light-sheet, as in the
31 original SPIM concept [38]; or by quickly scanning a thin laser beam through the focal
32 plane, thus resulting in a virtual light-sheet [46].

33 1.3.2 Static light-sheet illumination

34 For a static light-sheet, the normally circular Gaussian laser beam needs to be shaped
35 in an astigmatic manner, i.e. either expanded or squeezed along one direction, to shape
36 it into a sheet instead of a beam. This effect can be achieved by using a cylindrical lens,

1. LIVE IMAGING IN THREE DIMENSIONS

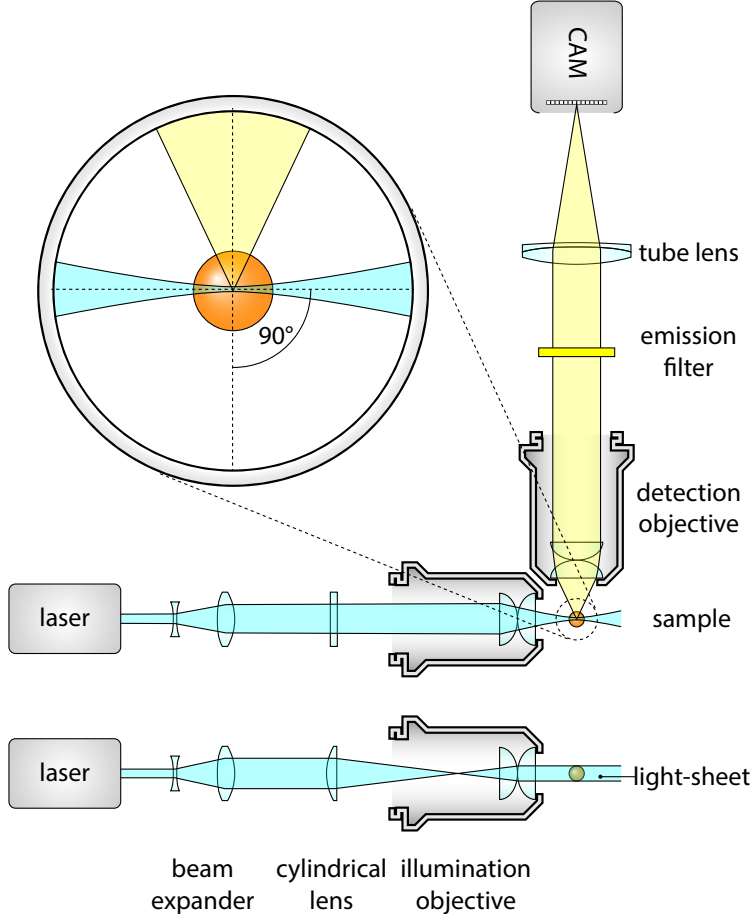


Figure 1.11: Basic optical components of a SPIM. A dedicated illumination objective is used to generate the light sheet, which is an astigmatic Gaussian beam, focuses along one direction. Astigmatism is introduced by placing a cylindrical lens focusing on the back focal plane of the objective. Detection is performed at a right angle, with a second, detection objective. Scattered laser light is filtered, and a tube lens forms the image on an area sensor, such as an sCMOS camera.

¹ which as the name suggests has a curvature in one direction, but is flat in the other, thus
² focusing a circular beam to a sheet.

³ However, to achieve light-sheets that are thin enough, one would need to use cylindrical lens with a very short focal length, and these are hardly accessible in well corrected formats. For this reason, it's more common to use a longer focal length cylindrical lens in conjunction with a microscope objective, which is well corrected for chromatic and spherical aberrations [53]. This way, the light-sheet length, thickness and width can be adjusted for the specific imaging tasks.

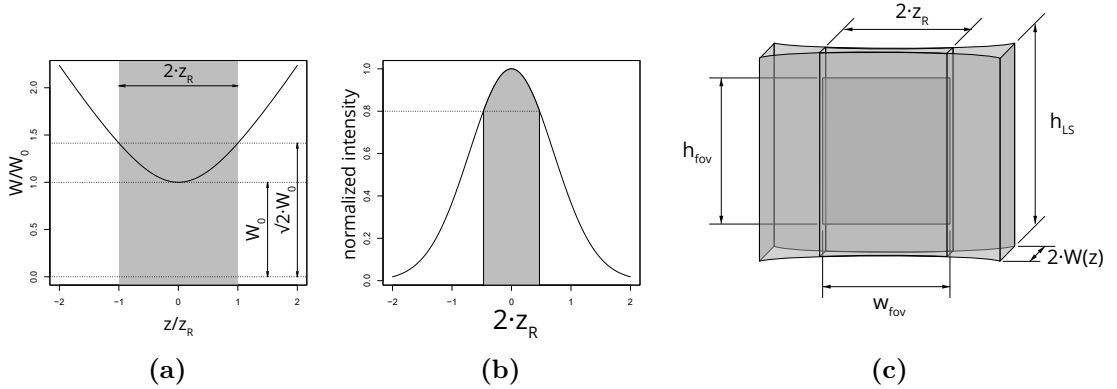


Figure 1.12: Light-sheet dimensions. 1.12a The width and thickness of the field of view depends on the Rayleigh length of the beam ($z_{R,y}$) and the beam waist (W_0). 1.12b Height of the field of view is determined by the Gaussian profile of the astigmatic beam. 1.12c shows a light sheet, with the field of view indicated. Since the light-sheet intensity is uneven, the field of view has to be confined to a smaller region.

1 Light-sheet dimensions

2 The shape of the illumination light determines the optical sectioning capability and the
 3 field of view of the microscope, so it is important to be able to quantify these measures.
 4 The most commonly used illumination source is a laser beam coupled to a single mode
 5 fiber, thus its properties can be described by Gaussian beam optics.

6 For paraxial waves, i.e. waves with nearly parallel wave front normals, a general wave
 7 equation can be approximated with the paraxial Helmholtz equation [54]

$$\nabla_T^2 U + i2k \frac{\partial U}{\partial z} = 0 \quad (1.17)$$

8 where $\nabla_T^2 = \frac{\partial^2}{\partial x^2} + \frac{\partial^2}{\partial y^2}$, $U(\vec{r})$ is the wave function, $k = \frac{2\pi}{\lambda}$ is the wavenumber and z is in
 9 the direction of the light propagation.

10 A simple solution to this differential equation is the Gaussian beam:

$$U(r, z) = A_0 \cdot \frac{W_0}{W(z)} \cdot e^{-\frac{r^2}{W^2(z)}} \cdot e^{-i \cdot \phi(r, z)} \quad (1.18)$$

11 where A_0 is the amplitude of the wave, W_0 is the radius of the beam waist (the thinnest
 12 location on the beam), $r = \sqrt{x^2 + y^2}$ is the distance from the center of the beam, $W(z)$
 13 is the radius of the beam z distance from the waist, and $\phi(r, z)$ is the combined phase
 14 part of the wave-function (Fig. 1.12a). Furthermore:

$$W(z) = W_0 \sqrt{1 + \left(\frac{z}{z_R}\right)^2} \quad (1.19)$$

1. LIVE IMAGING IN THREE DIMENSIONS

1 where the parameter z_R is called the Rayleigh-range, and is defined the following way:

$$z_R = \frac{\pi W_0^2}{\lambda}. \quad (1.20)$$

2 Apart from the circular Gaussian beam, the elliptical Gaussian beam is also an eigen-
3 function of Helmholtz equation (1.17) which describes the beam shape after a cylindrical
4 lens:

$$U(x, y, z) = A_0 \cdot \sqrt{\frac{W_{0,x}}{W_x(z - z_{0,x})}} \sqrt{\frac{W_{0,y}}{W_y(z - z_{0,y})}} \cdot e^{-\frac{x^2}{W_x^2(z - z_{0,x})}} \cdot e^{-\frac{y^2}{W_y^2(z - z_{0,y})}} \cdot e^{-i \cdot \phi(x, y, z)} \quad (1.21)$$

This beam still has a Gaussian profile along the x and y axes, but the radii ($W_{0,x}$ and $W_{0,y}$), and the beam waist positions ($z_{0,x}$ and $z_{0,y}$) are uncoupled, which results in an elliptical and astigmatic beam. The beam width can be now described by two independent equations for the two orthogonal directions:

$$W_x(z) = W_{0,x} \sqrt{1 + \left(\frac{z}{z_{R,x}}\right)^2} \quad \text{and} \quad W_y(z) = W_{0,y} \sqrt{1 + \left(\frac{z}{z_{R,y}}\right)^2}. \quad (1.22)$$

Since the beam waist is different along the two axes, the Rayleigh range is also different:

$$z_{R,x} = \frac{\pi W_{x,0}^2}{\lambda}, \quad z_{R,y} = \frac{\pi W_{y,0}^2}{\lambda}. \quad (1.23)$$

5 Based on these equations, the light-sheet dimensions and usable field of view (fov)
6 can be specified (Fig. 1.12c). The light-sheet thickness will depend on the beam waist,
7 $W_{0,y}$ (if we assume the cylindrical lens is focusing along y), and the length of the light-
8 sheet can be defined as twice the Rayleigh range, $2 \cdot z_{R,y}$. As these are coupled (see Eq.
9 1.23), having a thin light-sheet for better sectioning also means the length of it will be
10 relatively short. Fortunately, because of the quadratic relation, to increase the field of
11 view by a factor of two, the light-sheet thickness only needs to increase by a factor of
12 $\sqrt{2}$.

13 Light-sheet height is determined by the intensity profile of the beam along the vertical
14 axis (Fig. 1.12b). Since this is a Gaussian function (see Eq. 1.18), only a small part in
15 the middle can be used for imaging, because towards the sides the intensity dramatically
16 drops. To allow a maximum 20% drop of intensity at the edges, the light-sheet height is
17 $h_{fov} = 2 \cdot 0.472 \cdot W_{x,0}$.

18 1.3.3 Digitally scanned light-sheet illumination

19 Although generating a static light-sheet is relatively straightforward, with the simple
20 addition of a cylindrical lens to the light path, it has some drawbacks. As already men-

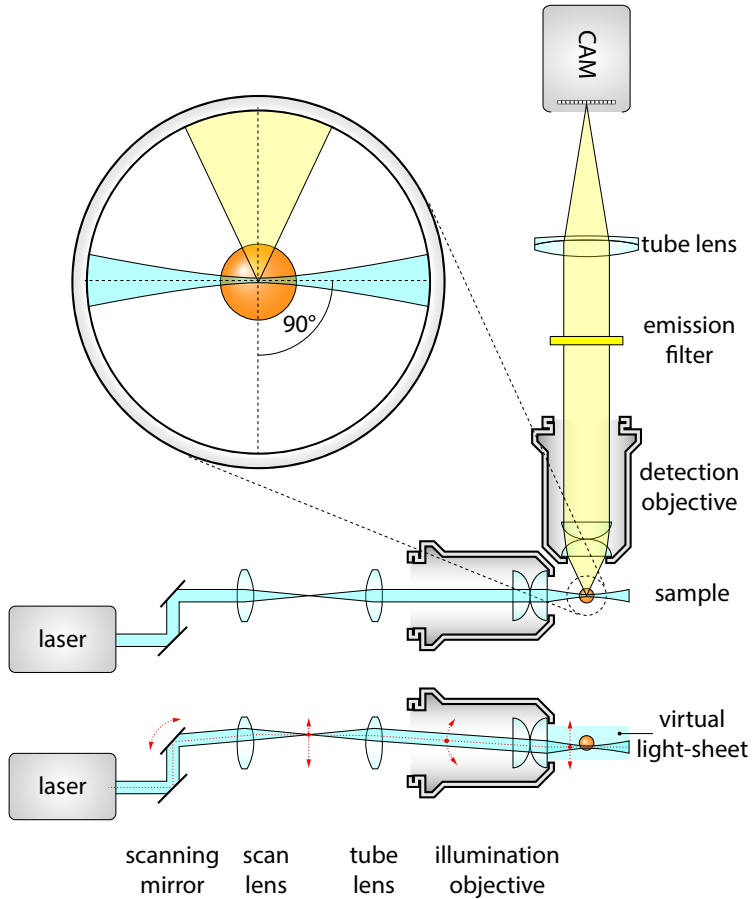


Figure 1.13: DSLM illumination. DSLM illuminates a specimen by a circularly-symmetric beam that is scanned over the field of view. This creates a virtual light-sheet, which illuminates a section of a specimen just like the SPIM. Light-sheet in DSLM is uniform over the whole field of view and its height can be dynamically altered by changing the beam scan range.

tioned in the previous section, the light intensity distribution along the field of view is not constant, as the light-sheet is shaped from a Gaussian beam. Furthermore, along the lateral direction of the light-sheet the illumination NA is extremely low, resulting in effectively collimated light. Because of this, shadowing artifacts can deteriorate the image quality [42].

A more flexible way of creating a light-sheet is by scanning a focused beam in the focal plane to generate a virtual light-sheet (digital scanned light-sheet microscopy, DSLM [46]). Although this method might require higher peak intensities, it solves both drawbacks of the cylindrical lens illumination. By scanning the beam, the light-sheet height can be freely chosen, and a homogenous illumination will be provided. Focusing the beam in all directions evenly introduces more angles in the lateral direction as well, which shortens the length of the shadows.

The basic optical layout of a DSLM is shown on Fig. 1.13. A galvanometer controlled

1. LIVE IMAGING IN THREE DIMENSIONS

1 mirror is used to alter the beam path that can quickly turn around its axis which will
2 result in an angular sweep of the laser beam. To change the angular movement to trans-
3 lation, a scan lens is used to generate an intermediate scanning plane. This plane is then
4 imaged to the specimen by the tube lens and the illumination objective, resulting in a
5 scanned focused beam at the detection focal plane. The detection unit is identical to the
6 wide-field detection scheme, similarly to the static light-sheet illumination. By scanning
7 the beam at a high frequency, a virtual light-sheet is generated, and the fluorescent signal
8 is captured by a single exposure on the camera, resulting in an evenly illuminated field
9 of view.

10 1.4 Light-sheet microscopy for mouse imaging

11 Because of its optical sectioning capabilities, combined with the high specificity of fluo-
12 rescent labels, confocal microscopy has been the go-to technique for decades in biological
13 research. Even though it has some drawbacks, important discoveries have been made
14 using this technique, as live imaging is not always necessary.

15 Especially using cell cultures, or fixed specimens, confocal microscopy has been
16 used to investigate X chromosome inactivation [55], the role of amyloid β -peptide in
17 Alzheimer's disease [56], the role of Oct4 [57] and Sox2 [58] in the self-renewal of pluripo-
18 tent stem cells, just to highlight a few.

19 Live imaging capabilities of confocal microscopy are, however, limited. This is mostly
20 due to the illumination scheme: to collect information from a single point, almost the
21 whole embryo has to be illuminated. This unwanted illumination can easily lead to
22 bleaching of the fluorophores, and also to phototoxic effects that can prevent further
23 embryonic development. The point scanning nature of image acquisition also implies an
24 inherent constraint to the maximum imaging speed, as it can be only increased at the
25 expense of reducing signal intensity (Fig. 1.1).

26 One improvement to address both of these drawbacks is the use of a spinning disk with
27 a specific pattern (also called Nipkow disk) of holes to generate multiple confocal spots
28 at the same time [59]. If these spots are far enough from each other, confocal rejection
29 of out-of-focus light can still occur. As the disk is spinning, the hole pattern will sweep
30 the entire field of view, eventually covering all points [60]. The image is recorded by an
31 area detector, such as a CCD or EM-CCD, which speeds up image acquisition [61].

32 Although out-of-focus illumination is still an issue, spinning disk confocal microscopy
33 was successfully used to investigate the mechanisms of symmetry breaking in early mouse
34 embryonic development [62], and the mechanisms leading to the first cell fate specification
35 that will differentiate extraembryonic tissue from the embryo proper [31, 63, 64]. Even
36 though these studies were carried out with live embryos, only a few hours of continuous

1 imaging is possible before the accumulation of phototoxic effects arrests development
2 [65]. Compared to this, just the pre-implantation phase of mouse embryonic development
3 spans 3 days, and the full development is 18 days [66].

4 1.4.1 Imaging pre-implantation

5 Pre-implantation is the first phase of mouse embryonic development, that starts right
6 after fertilization. The embryo in this phase is still in the oviduct, travelling towards
7 the uterus, where it will implant to the uterine wall. The developmental stage between
8 fertilization and the implantation is called the pre-implantation stage. Here the embryo
9 divides, and already the first cell fate specifications start when forming the trophoecto-
10 derm (TE) and the inner cell mass (ICM) at the blastocyst stage. ICM cells will form
11 the embryo proper, while TE cell will contribute to the formation of the extraembryonic
12 tissues.

13 During this process the embryo is still self-sufficient, which makes it possible to image
14 this stage in an *ex vivo* embryo culture by providing the proper conditions [67]. Long
15 term imaging, however, is extremely challenging due to the very high light sensitivity of
16 the specimens. Imaging these embryos in a confocal microscope will lead to incomplete
17 development, even if the imaging frequency is minimized to every 15 mins [J2].

18 Imaging for just a few hours is already enough to investigate important processes, such
19 as cell fate patterning [68]. Other approaches aim to lower the phototoxicity by either
20 using 2-photon illumination which operates at longer wavelengths [69–71], or by lowering
21 imaging frequency as a compromise [72]. These approaches, however either require highly
22 specialized equipment, such as an ultra short pulsed laser, or is compromising on the time
23 resolution.

24 Light-sheet microscopy, on the other hand, drastically lowers phototoxic effect by
25 using a much more efficient illumination scheme (see Sec. 1.3), and thus makes a better
26 use of the photon budget. Using this technique, it is possible to image the full pre-
27 implantation development at high spatial and temporal resolution without any negative
28 impact on the developmental process. Such a microscope was developed by Strnad *et al.*
29 at EMBL [J2], who used it to understand when exactly is the first cell fate specification
30 decided in the embryonic cells.

31 As a mouse embryo culture is not compatible with the standard agarose-based sample
32 mounting techniques, a completely new approach was taken, which resulted in a micro-
33 scope designed around the sample. The sample holder forming a V-shape was built with
34 a bottom window, and it is lined with a thin FEP (fluorinated ethylene propylene) foil
35 that supports the embryos (Fig. 1.14A, i). This arrangement allows the utilization of
36 the standard microdrop embryo culture, while providing proper viewing access for the
37 objectives. As the embryos are relatively small (100 µm) and transparent, a single illu-

1. LIVE IMAGING IN THREE DIMENSIONS

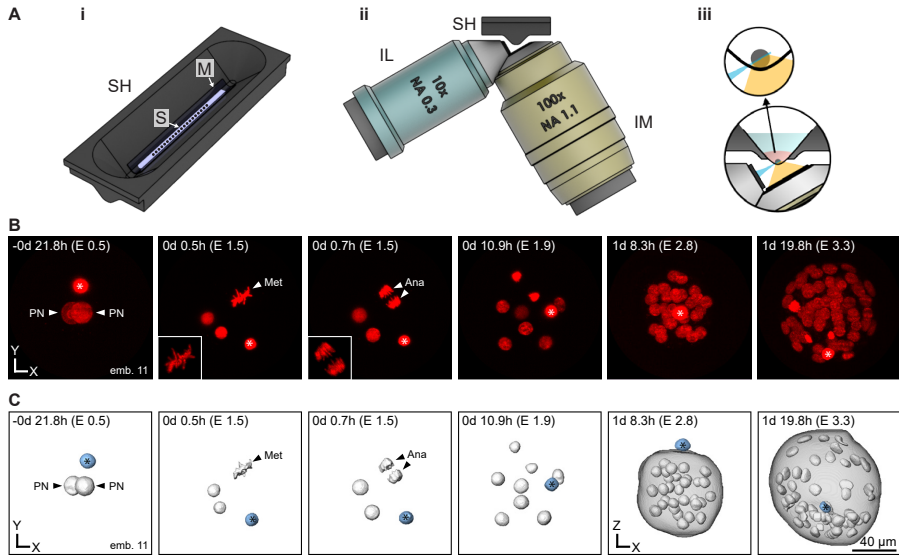


Figure 1.14: Inverted light-sheet microscope for multiple early mouse embryo imaging.. (i) A sample holder (SH), containing a transparent FEP membrane (M) allows multiple embryo samples (S) to be placed in line for multisample imaging. (ii) Inverted objective orientation with side view of the sample holder. One possible configuration is to use a 10×0.3 NA illumination objective (IL) and another 100×1.1 NA detection objective placed at a right angle to the illumination. (iii) Close up on side view of sample on FEP membrane with both objectives. Since the FEP membrane is transparent on water, it provides no hindrance to the illumination beam in penetrating the sample or for the emitted fluorescence on reaching the detection objective. (B) Still images of one particular timelapse experiment, and (C) corresponding segmented nuclei. The star depicts the polar body. Adapted from Strnad *et al.* [J2]

mination and single detection objective arrangement is enough for high quality imaging.
 2 A low resolution ($NA=0.3$) objective is used to generate the scanned light-sheet, and
 3 a high resolution ($NA=1.1$) objective is detecting the fluorescence at $50\times$ magnification
 4 (Fig 1.14A, ii). As the foil is curved, it allows unrestricted access to the embryo, while
 5 separating the imaging medium from the immersion liquid (Fig. 1.14A, iii). Furthermore,
 6 its refractive index is matching the refractive index of water, so optical aberrations are
 7 minimized.

Using this setup, Strnad *et al.* were able to pinpoint the exact timing of the first cell fate decision that leads either to ICM or TE cells. More than 100 embryos expressing nuclear (H2B-mCherry) and membrane (mG) markers were imaged for the entire 3 days of pre-implantation development (Fig. 1.14B). The image quality was good enough to segment all nuclei in the embryos (Fig. 1.14C), and track them from 1 to 64 cell stage, building the complete lineage tree. Based on the lineage trees, and the final cell fate assignments, it was determined that at the 16 cell stage the final specification is already decided, while earlier than this it is still random.

1.4.2 Imaging post-implantation development

After the initial 3 days of pre-implantation, the embryo undergoes the implantation process, during which it is inaccessible to microscopical investigations. Although a new

1.4 Light-sheet microscopy for mouse imaging

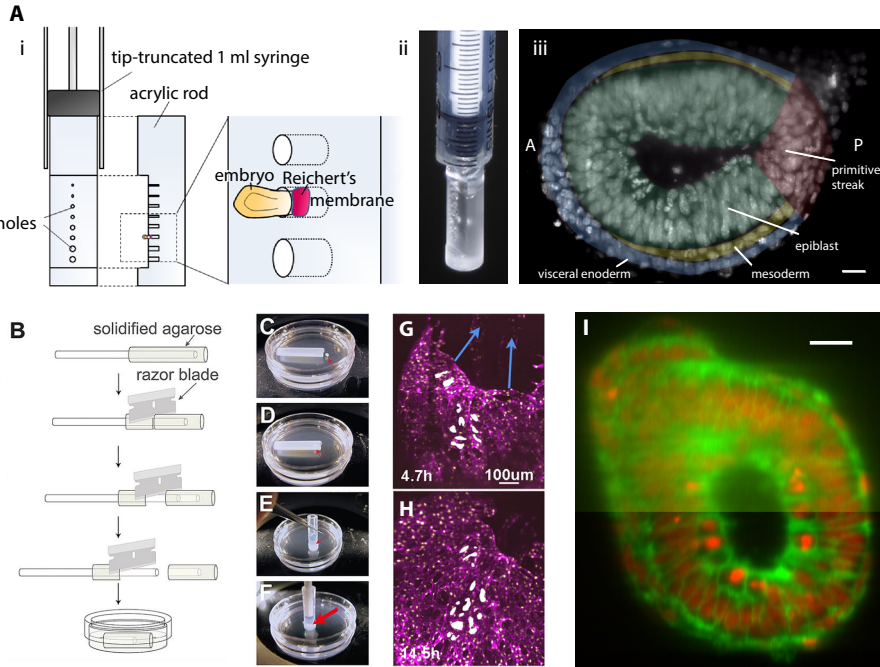


Figure 1.15: Imaging mouse post-implantation development. (A) (i, ii) Mounting technique for E5.5 to E6.5 embryos. A tip-truncated 1 mL syringe holds an acrylic rod, cut and drilled with holes of different size in order to best fit the mouse embryo by its Reichert's membrane, leaving the embryo free inside the medium. (iii) Maximum intensity projection of a 13 μm slice at 78 μm from distal end of an E6.5 mouse embryo. The different tissues corresponding to the rudimentary body plan are annotated. Scale bar: 20 μm . (B) For stages ranging between E6.5 and E8.5, mounting using a hollow agarose cylinder has also successfully been proposed. Optimal sizes for the corresponding embryonic stage to be imaged can be produced, so that the embryo can grow with least hindrance. (C–F) Steps for mounting the mouse embryo inside the agarose cylinder. The inner volume of the cylinder can be filled with optimal medium, allowing the much larger chamber volume to have less expensive medium. (G–H) Example images of a 9.8 h timelapse with the mounting shown in (B) where the expansion of the yolk sac can be observed in direction of the blue arrows. (I) In order to aid multiview light-sheet setups in overcoming the higher scattering properties of embryos at this stage, and to allow faster and easier data recording, electronic confocal slit detection allows better quality images to be taken at shorter acquisition times. Scale bar: 20 μm . Adapted from Ichikawa *et al.* [47], Udan *et al.* [48] and de Medeiros and Norlin *et al.* [73].

1 method was recently developed that allows *in vitro* culturing of the embryos embedded
2 in a 3D gel [74], this has not reached wider adoption yet. Because of this, developmental
3 processes during implantation have only been investigated in fixed embryos.

4 Following the implantation process, at the post-implantation phase, *ex vivo* embryo
5 culturing becomes possible again [75, 76], and these embryos can be kept alive for several
6 days in an artificial environment. During this process especially interesting stages are the
7 late blastocyst (~4.5), gastrulation (~E6.5), and somite formation (~E8.5). Before live
8 imaging techniques became available, these stages were mostly investigated using *in situ*
9 visualization techniques to shed light on several developmental processes [77]. Many
10 pathways playing important roles have been identified this way, however live imaging is
11 still necessary to validate these results, and ensure continuity in the same specimen [78].

12 Light-sheet microscopy is a good choice for imaging these stages, just like in the case
13 of pre-implantation embryos. These embryos, however, present new challenges for sample

1. LIVE IMAGING IN THREE DIMENSIONS

1 handling and culturing. Owing to their extreme sensitivity, dissection can be difficult,
2 especially for earlier stages (E4.5). Furthermore, since the embryo is also growing during
3 development, gel embedding is not an option, as this might constrain proper development.
4 Thus, special handling and mounting techniques had to be developed in order to allow
5 live 3D imaging of these specimens.

6 Ichikawa *et al.* [47] designed a custom mounting apparatus manufactured from acrylic
7 in the shape of a rod that fits in a standard 1 mL syringe with its tip truncated (Fig.
8 1.15A, i). In the rod several holes were drilled with different sizes that can accommo-
9 date different sized embryos, which are held by an extraembryonic tissue, the Reichert's
10 membrane (Fig. 1.15A, ii). Mounting this way doesn't disturb the embryo itself, and it
11 can freely develop in the culturing medium, while it is also stationary for the purpose of
12 imaging. Using this technique, Ichikawa *et al.* were able to image through several stages
13 of development, including interkinetic nuclear migration at stages E5.5–6.5 (Fig. 1.15A,
14 iii).

15 A second method of sample mounting for light-sheet imaging was developed by
16 Udan *et al.* who were able to record a full 24 h time-lapse of living embryos focusing
17 on the gastrulation and yolk sac formation processes (Fig. 1.15G–I). Their mounting
18 technique comprised of producing a hollow agarose container shaped like a cylinder that
19 could support the embryo from below without constraining its growth (Fig. 1.15B–F).

20 Another consideration to keep in mind, is the growing size of the embryo. As it gets
21 bigger, illumination is less efficient, and scattering can dominate at larger depths. As
22 mentioned in earlier (Sec. 1.3) this can be alleviated by multi-view imaging: illuminating
23 and detecting from multiple directions. Electronic confocal slit detection can further
24 improve the signal to noise ratio by rejecting unwanted scattered light, which allows
25 deeper imaging in large specimens, even up to E7.5 (Fig. 1.15I) [73].

26 1.4.3 Imaging adult mice

27 Imaging adult mice is especially interesting for answering neurobiological questions. Since
28 development is over at this stage, the use of an environmental chamber is no longer neces-
29 sary. The biggest challenge for imaging these samples is their size, as they are centimeters
30 in size instead of less than a millimeter in the embryonic stage. Furthermore, the tissues
31 of adult mice are much more opaque which severely limits imaging depth. Light-sheet
32 microscopy can already deal with large specimens, however to achieve (sub)cellular res-
33 olution for an entire brain for example, multiple recording have to be stitched together
34 after acquisition [79].

35 Light scattering and absorption depends on the tissue composition, and also imaging
36 depth. Especially the brain with the high concentration of lipids in the myelinated fibers
37 pose a real challenge for imaging. Live imaging is usually performed with 2-photon mi-

1.4 Light-sheet microscopy for mouse imaging

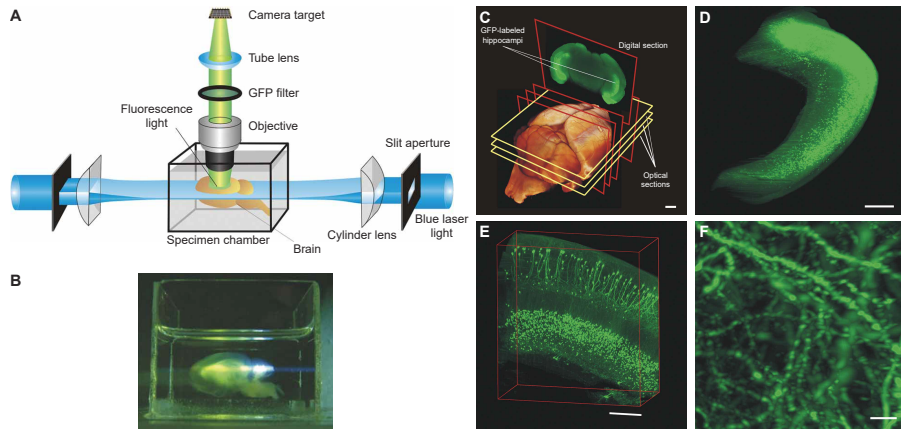


Figure 1.16: Imaging adult mouse brain with light-sheet microscopy.. (A) Schematics of the ultramicroscope for brain imaging. The specimen is embedded in clearing medium to ensure necessary imaging depth. Illumination is applied from two sides to achieve even illumination for the whole field of view. Light-sheet is generated by a slit aperture flowed by a cylindrical lens. The specimen is imaged from the top using wide-field detection method. (B) Photograph of the imaging chamber with a mounted cleared specimen and light-sheet illumination. (C) Surface rendering of a whole mouse brain, reconstructed from 550 optical sections. GFP and autofluorescence signal was imaged. Hippocampal pyramidal and granule cell layers are visible in the digital section. Scale bar: 1 mm. Objective: Planapoachromat 0.5 \times . (D) Reconstruction of an excised hippocampus from 410 sections. Note that single cell bodies are visible. Scale bar: 500 μ m. Objective: Fluar 2.5 \times . (E) 3D reconstruction of a smaller region of an excised hippocampus from 132 sections. Scale bar: 200 μ m. Objective: Fluar 5 \times . (F) 3D reconstruction of CA1 pyramidal cells imaged with a higher resolution objective (LD-Plan Neofluar 20 \times NA 0.4) in a whole hippocampus (430 sections). Dendritic spines are also visible, even though usually a higher NA objective (>1.2) is required to visualize these. Scale bar: 5 μ m. Adapted from Dodt *et al.* [5].

1 microscopy which can penetrate the tissue up to 800 μ m [80]. Using fixed samples, however,
2 the scattering problem can be eliminated by the use of tissue clearing methods.

3 Tissue clearing is a process that removes and/or substitutes scattering and absorbing
4 molecules by a chemical process while keeping the tissue structure intact and preserving
5 fluorescence. The most dominant contributors to these effects are the proteins and lipids.
6 Proteins in the cells locally change the refractive index of the tissue which leads to
7 scattering, while lipids absorb the light. Clearing methods tackle these problems by
8 chemically removing and substituting lipids by certain types of gel, and immersing the
9 whole sample in a medium with higher refractive index to match the optical properties
10 of proteins. Numerous methods have been developed for tissue clearing, such as ScaleA2
11 [81], 3DISCO [82, 83], ClearT2 [84], SeeDB [85], CLARITY [86, 87], CUBIC [88] and
12 iDISCO [89].

13 The first combination of optical clearing and light-sheet microscopy for whole brain
14 imaging was performed by Dodt *et al.* using a custom ultramicroscope consisting of two
15 opposing illumination arms and a single detection with an objective from above (Fig.
16 1.16A). The light-sheets were positioned horizontally, and the cleared samples could be
17 placed in a transparent imaging chamber filled with the clearing medium (Fig. 1.16B).
18 Imaging was performed from both top and bottom after rotating the sample 180°. By
19 changing the detection lens, it is possible to adapt the system to different samples:

1. LIVE IMAGING IN THREE DIMENSIONS

1 low magnification is capable of imaging the whole brain (Fig. 1.16C), while for smaller,
2 dissected parts, such as the hippocampus, higher magnification with higher resolution is
3 more appropriate (Fig. 1.16D). With this configuration individual cell-cell contacts can
4 be recognized (Fig. 1.16E), and even dendritic spines can be visualized (Fig. 1.16F).

5 Although light-sheet microscopy is highly suitable for imaging cleared specimens, even
6 entire mice [90], brain imaging in live animals is more challenging due to the standard
7 two-objective setup of a conventional SPIM microscope. Two light-sheet based methods,
8 however offer a solution for this, axial plane optical microscopy (APOM) [91] and swept
9 confocally-aligned planar excitation (SCAPE) [92] both use only a single objective to
10 generate a light-sheet and detect the fluorescence as well. This is done by rotating the
11 detection plane at an intermediate image (APOM), or by rotating both the light-sheet
12 and detection plane simultaneously (SCAPE).

¹ Chapter 2

² Dual Mouse-SPIM

³ 2.1 Challenges in imaging mouse pre-implantation development

⁵ mammalian development chromosome segregation cell specification symmetry breaking
⁶ signaling pathways human infertility congenital diseases
⁷ current mouse-SPIM [J2] already is very good for answering many of these questions
⁸ advantages: immersion liquid and culture medium separated open-top sample holder
⁹ allow standard microdrop *in vitro* embryo culture row of embryos - high throughput dual
¹⁰ color imaging environmental chamber allows live imaging for 3 days, every
¹¹ follow chromosomes by tracking kinetochores
¹² from lattice paper: “because photodamage mechanisms that scale supralinearly with
¹³ peak intensity have been identified for both visible [93] and two-photon [94] excitation.”

¹⁴ 2.2 Microscope design principles

¹⁵ In order to address the challenges outlined in the previous section, we propose a new light-
¹⁶ sheet microscope design for imaging pre-implantation development at high resolution.
¹⁷ The design is guided by the following requirements:

- ¹⁸ 1. subcellular, isotropic resolution
- ¹⁹ 2. high light collection efficiency
- ²⁰ 3. live embryo compatible

²¹ From these requirements the strongest is the live compatibility

²² 2.2.1 Light collection efficiency of an objective

²³ Resolution is not the only parameter of concern when designing a new microscope setup.
²⁴ We also have to consider light collection efficiency, since many application, especially

2. DUAL MOUSE-SPIM

1 live imaging applications require a tight photon budget. This means a single fluorophore
2 can only emit so many times before it undergoes an irreversible chemical reaction, i.e. it
3 bleaches. The more we can collect of these photons, the more information we gain, and
4 altogether the efficiency is higher.

5 Photon collection efficiency also defines single molecule localization accuracy, since
6 the signal to noise ratio will depend on the square of the number of collected photons.
7 This is why it's important to also maximize light collection efficiency.

8 Let's define light collection efficiency η as the ratio of collected photons and all
9 emitted photons:

$$\eta = \frac{N_{\text{collected}}}{N_{\text{emitted}}}$$

10 Since we can assume that the direction of photons emitted from a fluorescent molecule
11 are random, the light collection efficiency will correspond to the solid angle subtended
12 by the objective front lens at the focal point. To calculate this, let's consider the unit
13 sphere centered at the focal point, and calculate the surface area of the spherical cap
14 corresponding to the objective acceptance angle α (Fig. 2.1a). The area of the cap can
15 be expressed as a function of the angle:

$$A_{\text{cap}} = 2\pi r^2(1 - \cos \alpha)$$

16 The surface area of the full sphere is calculated as:

$$A_{\text{sph}} = 4\pi r^2$$

17 For both equations r is the radius of the sphere. From here, the light collection efficiency
18 can be calculated as:

$$\eta = \frac{N_{\text{collected}}}{N_{\text{emitted}}} = \frac{A_{\text{cap}}}{A_{\text{sph}}} = \frac{1 - \cos \alpha}{2}$$

19 Some more calculations: (Fig. 2.1b).

20 2.2.2 Multi-view resolution

21 here a figure with rotating 2 psfs

22 2.3 Optical layout

23 design principles: highest isotropic resolution, highest light collection efficiency possible
24 2x0.8 NA water dipping in 90° multi-view deconvolve Gaussian fit $\sigma_{xyz} = 135$ 2x1.1 NA
25 water dipping in 120° multi-view deconvolved Gaussian fit $\sigma_z = 135$, and $\sigma_{xy} = 82.2$
26 simulations from PSF generator! put here

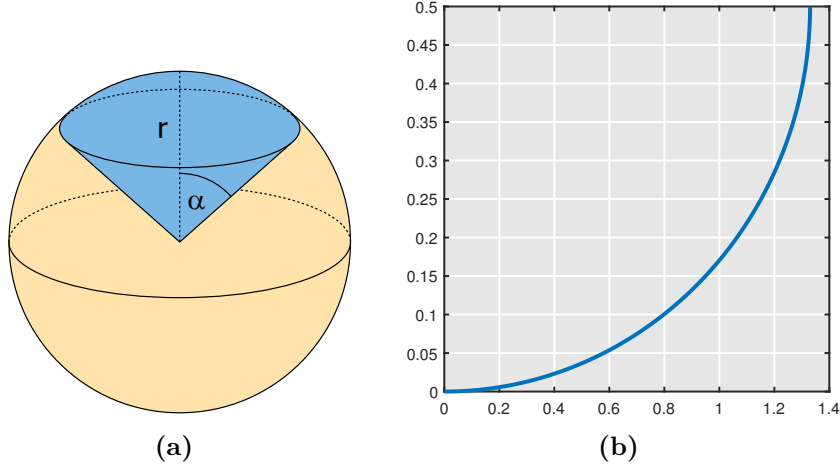


Figure 2.1: Light collection efficiency of an objective. (a) Light collection efficiency is the ratio of photons collected by the objective and all emitted photons. If the fluorophores are emitted randomly in all directions, it will be the surface ratio of the conical section (blue) to the whole sphere. (b) Light collection efficiency (η) as a function of the numerical aperture (NA)

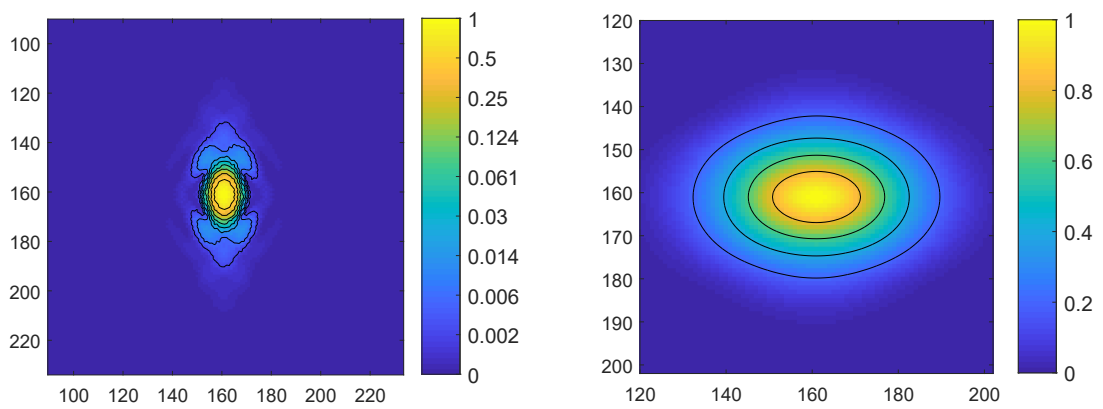


Figure 2.2: Axial cross section of the PSF and OTF of a multi-view single plane illumination microscope. Simulated PSF and OTF for a single plane illumination microscope with a water immersion objectives ($n = 1.33$). Multi-view image acquisition at 120° was simulated. Detection: $NA = 1.1$, $\lambda = 510$ nm, Illumination: $NA = 0.1$, $\lambda = 488$ nm

2. DUAL MOUSE-SPIM

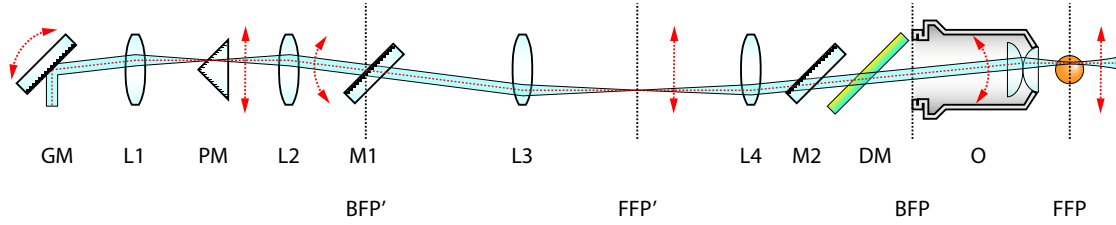


Figure 2.3: Simplified schematics for illumination.

- 1 When designing the optical layout of the setup, we had two principles in mind:
- 2 simplicity and efficiency. Because of the symmetrical design it is possible that

3 2.3.1 Illumination

4 Beam splitter unit

5 2.3.2 Detection

6 Light combining unit

7 2.4 Optical alignment

8 Precise alignment of the illumination and detection paths are crucial for high quality
9 imaging, and has a pronounced importance for high magnification and high resolution
10 optical systems. The DualMouse SPIM contains two illumination and detection paths
11 that share many common elements, which makes alignment a *important?* process. The
12 final aim for the alignment is to perfectly overlap the light-sheets with the detection focal
13 planes, and to optimize ...

14 2.4.1 Alignment of illumination branches

15 The two illumination branches start with a common light source, a single mode fiber
16 coupled to laser combiner, and they also share a galvanometric mirror that performs the
17 beam scanning to generate the virtual light-sheet. Likewise shared is a scan lens focusing
18 on the galvo mirror (GM), and the illumination splitter unit (PM, see Section 2.3.1).

19 Alignment for the illumination arms are done in three steps. First the laser beam
20 is aligned on the first rail that holds the galvo, lens L1, and the splitter unit PM. This
21 is performed by two kinematic mirrors placed between the fiber output and the galvo
22 mirror. Using these two mirrors it's possible to freely align the beam along all 4 degrees
23 of freedom: translation in two orthogonal directions, and rotation around two orthogonal
24 axes. Beam alignment on the rail is tested by two irises at the two ends of the rail, if the
25 beam passes through both of them we consider it centered and straight on the optical
26 axis.

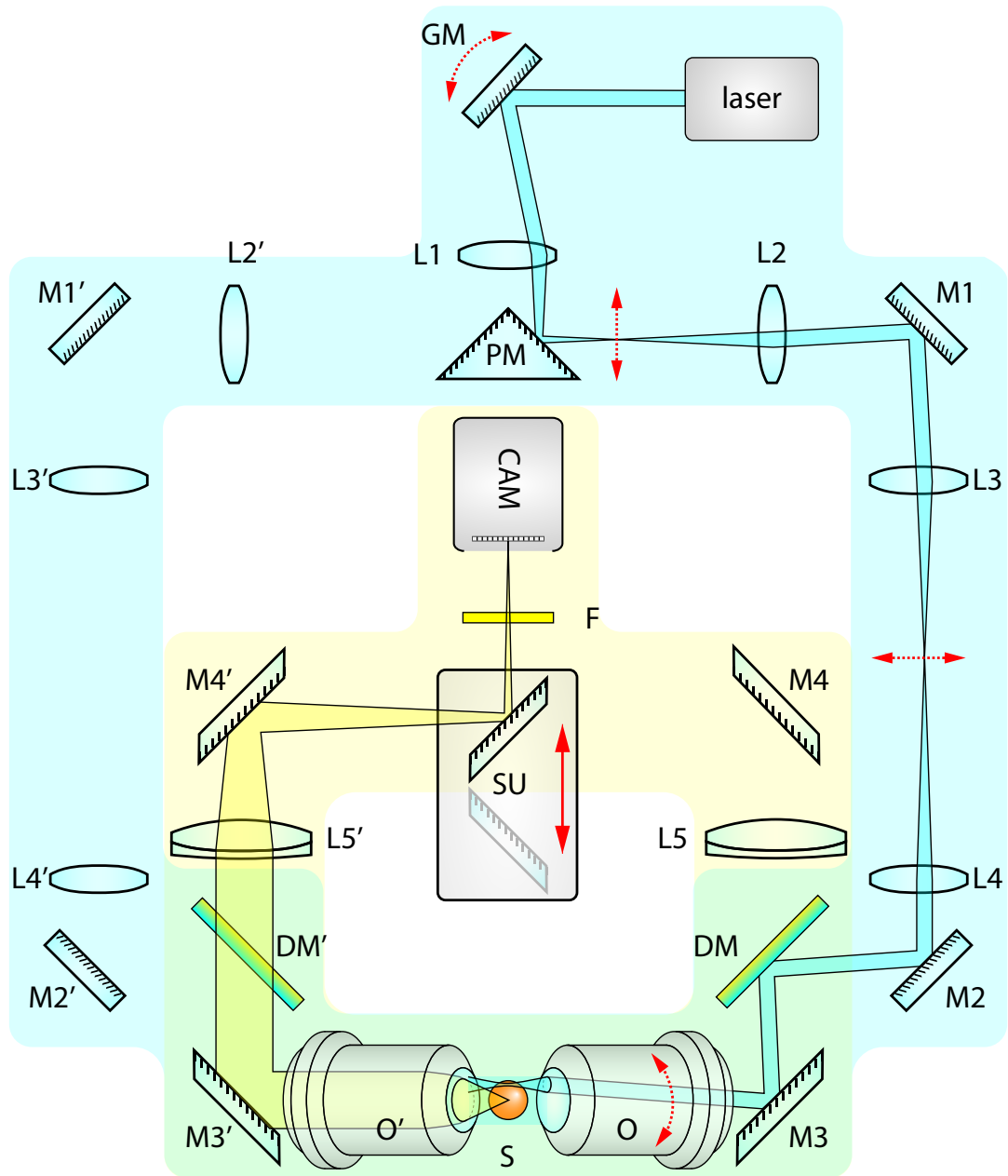


Figure 2.4: Dual Mouse SPIM optical layout. The microscope consists of two main parts, the illumination branches (blue) and detection branches (yellow). For both illumination and detection there are two identical paths implemented. Illumination direction can be changed by applying a different offset to the galvo mirror, which in turn will direct the beam to the opposite face of the prism mirror. L1 and L2 will then image the galvo on M1. Using L3 as a scan lens, and L4 as a tube lens, the scanned beam is coupled to the objective path by quad band dichroic mirror (DM) CAM – camera, DM – dichroic mirror, F – filter wheel, L – lens, M – mirror, O – objective, PM – prism mirror, S – sample, SU – switcher unit

- 1 After the beam is aligned on the first rail, lens L1 and the splitter unit PM are placed
- 2 in the measured positions to image the galvo mirror on mirror M1 using lenses L1 and
- 3 L2. Correct positioning of the splitter unit along the rail is crucial, since this will affect

2. DUAL MOUSE-SPIM

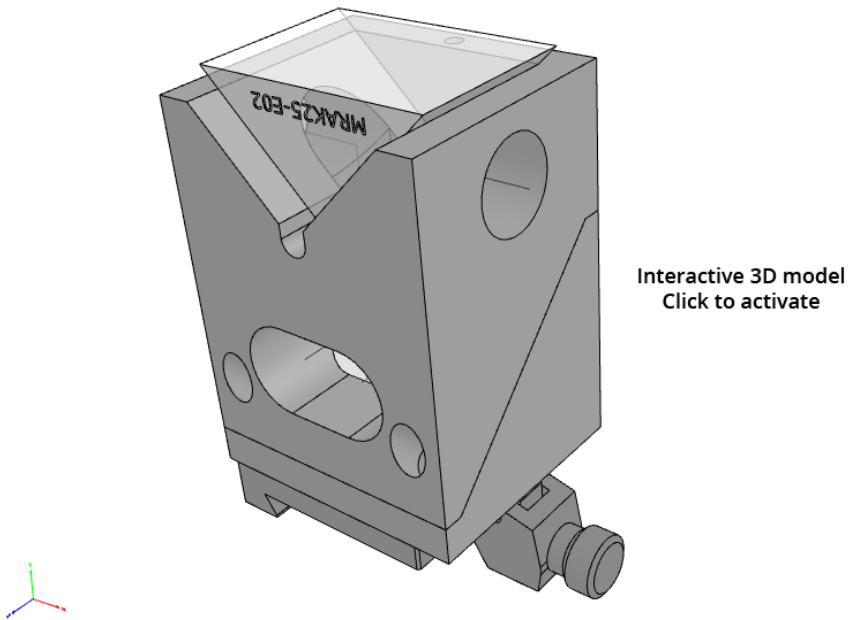


Figure 2.5: Illumination branch splitting block. 3D model of the custom designed splitter block used in the illumination branch. Depending on the horizontal beam position at the lower port, the beam will be reflected either to the right or to the left. Because of the mirror alignment, the beam is rotated 90 degrees.

- 1 the lateral position and tilt of the beam exiting the unit. To some extent, this can also
- 2 be compensated by adjusting the two mirrors before the galvo mirror, but is avoided if
- 3 possible as this will also displace the beam from the center of the galvo mirror.

4 Adjusting beam position.

- 5 Beam position can be adjusted by either translating the beam in a conjugated image
- 6 plane, or by rotating the beam in a conjugated back focal plane. The setup was designed
- 7 in a way, that BFP' coincides with mirror M2. This mirror is mounted in a gimbal mirror
- 8 mount, allowing to rotate the mirror exactly around its center, which avoids unwanted
- 9 translational movements, and results in pure rotation of the beam. Lens L3 is positioned
- 10 exactly 1 focal length from the mirror, thus acting as a scan lens, and transforming the
- 11 rotational movements to translation. This translation is further imaged and demagnified
- 12 by the tube lens L4 and the objective O.

- 13 **Adjusting beam tilt** Beam tilt can be adjusted by

14 Adjusting beam axial position.

- 15 **Adjusting scanning plane angle.** After the beam is properly aligned, i.e. it is in
- 16 focus, and in the center of field of view, it is still necessary to check if the scanning

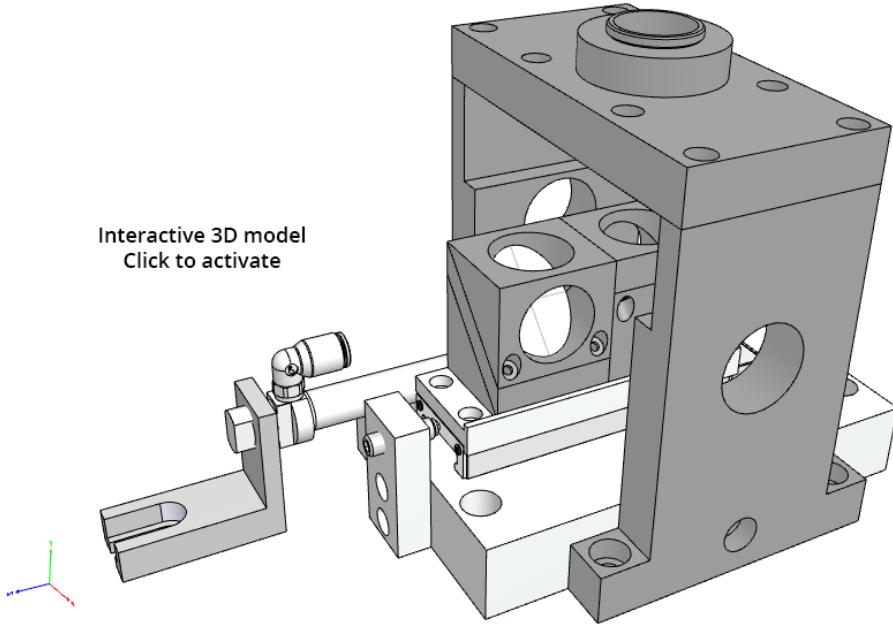


Figure 2.6: 3D model of the custom designed unit to enable quick switching between the two detection paths. A high precision stainless steel stage holds two mirror blocks facing opposite directions, and bouncing the light upwards, towards the camera. The units are translated by pneumatic cylinder to ensure high speed and reproducibility.

1 direction is parallel to the imaging plane. It is possible that the beam is in focus in the
 2 center position, but when moved up or down it drifts out of focus due to a tilted scanning
 3 angle. This tilt can be compensated by mirror M1, that is placed at the conjugated back
 4 focal plane BFP'. Between lenses L3 and L4 a magnified version of the light-sheet will
 5 be visible, and the tilt can be checked by placing an alignment target in the optical path
 6 while scanning the beam. By tilting mirror M1 up or down, the scanning pattern not only
 7 moves up or down, but is also rotated if the mirror surface is not exactly vertical. Since
 8 M1 and GM are in conjugated planes, the tilt and offset can be performed independently.
 9 The tilt is first fixed by M1 while inspecting the target, and the beam is re-centered by
 10 changing the offset on the galvo mirror. Moving the galvo mirror will not introduce tilt,
 11 since in this case rotation axis is perpendicular to the reflection plane.

12 2.4.2 Alignment of detection branches

13 Since the detection path is equivalent to a wide-field detection scheme, its alignment is
 14 much simpler than that of the illumination branches. The only difference is the detection
 15 branch merging unit (see Sec. 2.3.2.) that features two moving mirrors. This, however
 16 doesn't effect the alignment procedure, since the movement direction is parallel to both
 17 mirror's surface, meaning that the exact position of the mirrors will not affect the im-
 18 age quality, as long as the mirrors are not clipping the image itself. Stability test were

2. DUAL MOUSE-SPIM

1 performed to confirm the consistent switching performance of the mirror unit before the
2 final alignment took place (see Sec. 2.5.3).

3 The final alignment procedure

4 **Positioning the tube lens.** The position of the tube lens determines the focal plane
5 the is being imaged on the camera sensor. Ideally, the tube lens' distance from the
6 camera sensor is exactly the tube lens focal length, which will ensure the best imaging
7 performance. If the tube lens distance is not correct, the focal plane will be slightly shifted
8 in the axial direction. Although small shifts will not necessarily have detrimental effect
9 on the image quality, because the light sheet can also be shifted accordingly. Because
10 of the shifted focal and image planes, however, the magnification of the system will be
11 affected, and will change depending on the amount of defocus. For this reason we aim
12 for positioning the tube lens as close to the theoretical position as possible.

13 Our tube lens is a compound, achromatic lens with a center thickness of 12.5 mm, and
14 edge thickness of 11.3 mm. Its effective focal length is 400 mm which will produce a 50x
15 magnified image. Back focal length is 394.33 mm which we measured form the camera
16 chip, and the lens was positioned at this theoretically optimal position.

17 **Adjusting correction collar.** The Nikon 25x objectives used for this setup have
18 a built in correction ring that can be used to correct spherical aberrations resulting
19 from refractive index differences when imaging samples behind a coverslip. This can
20 be also effectively used to correct for any spherical aberrations occurring from imaging
21 through the FEP foil. Although these aberrations are expected to be extremely low, due
22 to the relatively thin, 50 μm foil thickness, and the close matching of refractive index
23 ($n_{FEP} = 1.344$, $n_{H_2O} = 1.333$), for optimal, aberration free image quality it can't be
24 neglected.

25 The correction collars are adjusted by inspecting a gel suspended fluorescent bead
26 specimen with the microscope, where the beads can act as a reporter of the point spread
27 function of the microscope. The alignment can be performed "live" by inspecting the
28 bead image quality for any aberrations. By gradually changing the correction collar, the
29 ring are minimized on out of focus beads, and the peak intensity is maximized for in
30 focus beads. By moving the correction ring, the focal plane is also slightly shifted, which
31 has to be compensated by shifting the light-sheet correspondingly to coincide with the
32 correct imaging plane.

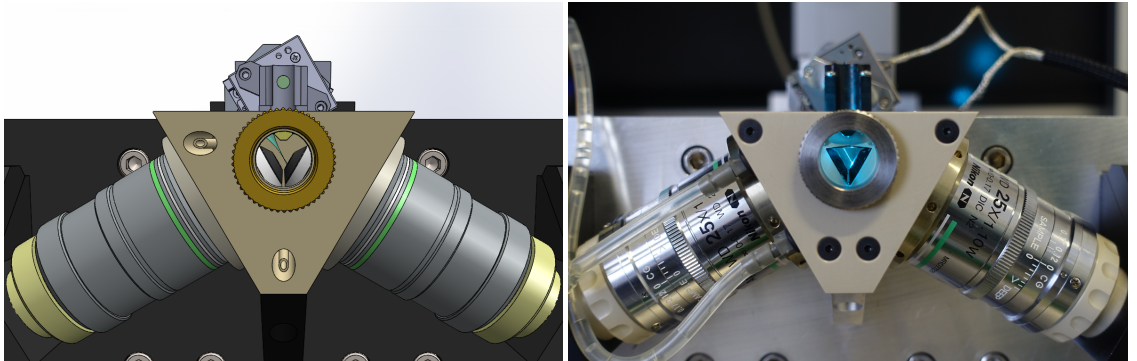
33 **Adjusting field of view.** To allow for proper sampling of the image, we use 50x
34 magnification, which, combined with the 6.5 μm pixel pitch of our sCMOS camera will
35 result in a 0.13 μm pixel size. The full field of view with this magnification is $2048 \times 0.13 =$
36 266.24 μm . The full field of view the objective provide, are larger than this, at 800 μm .

1 To ensure the best image quality, we align the center of the objective field of view on
 2 the camera sensor, since this region has the best optical properties in term of numerical
 3 aperture, aberration correction and field flatness.

4 Field of view alignment can be performed using mirror M4 just before the detection
 5 merging unit. To identify the center region of the field of view, diffuse white light is used
 6 to illuminate the entire sample chamber, and is imaged on the camera. Then, mirror M4 is
 7 adjusted until the top edge of the field of view becomes visible, *i.e.* where the illumination
 8 from the chamber is clipped. This will have a circular shape. Then, adjusting the mirror
 9 in the orthogonal direction, the left-right position of the field of view can be adjusted,
 10 by centering the visible arc on the camera sensor.

11 After the horizontal direction is centered, vertical centering is performed. This, how-
 12 ever can't be centered the same way as the horizontal direction, since for that we would
 13 have to misalign the already aligned horizontal position. To determine the center, we
 14 move the field of view from the topmost position to the bottom. During this process
 15 the number of turns of the adjustment screw is counted (this can be done accurately by
 16 using a hex key). After reaching the far end of the field of view, the mirror movement is
 17 reversed, and the screw is turned halfway to reach the middle.

18 2.5 Results



(a) Rendering of SolidWorks design.

(b) Photo of constructed microscope.

Figure 2.7: Front view of the Dual Mouse-SPIM.

19 Resolution for Lattice light-sheet [6]: 230 nm in x and 370 nm in z [44]

20 After the design phase, all custom parts were manufactured at the EMBL workshop,
 21 and I assembled the microscope on a NewPort X by X optical table (Fig. 2.7).

2. DUAL MOUSE-SPIM

1 2.5.1 Characterizing illumination profile

2 Since a Gaussian beam is used for illumination, it's intensity profile is dependent on the
3 axial position (Eq. 1.18). Although the total intensity at any cross section of the beam
4 is constant, because of the divergent properties, the peak intensity varies. To assess any
5 non-uniformities in the illumination pattern, I measured the illumination beam intensity
6 for each view.

7 To visualize the beam, the chamber was filled with a fluorescent solution (methylene
8 blue solution in distilled water). In order to increase the signal to noise ratio of these
9 images, a long exposure time of 200 ms were used, and 500 images of each beam was
10 averaged (Fig. 2.8).

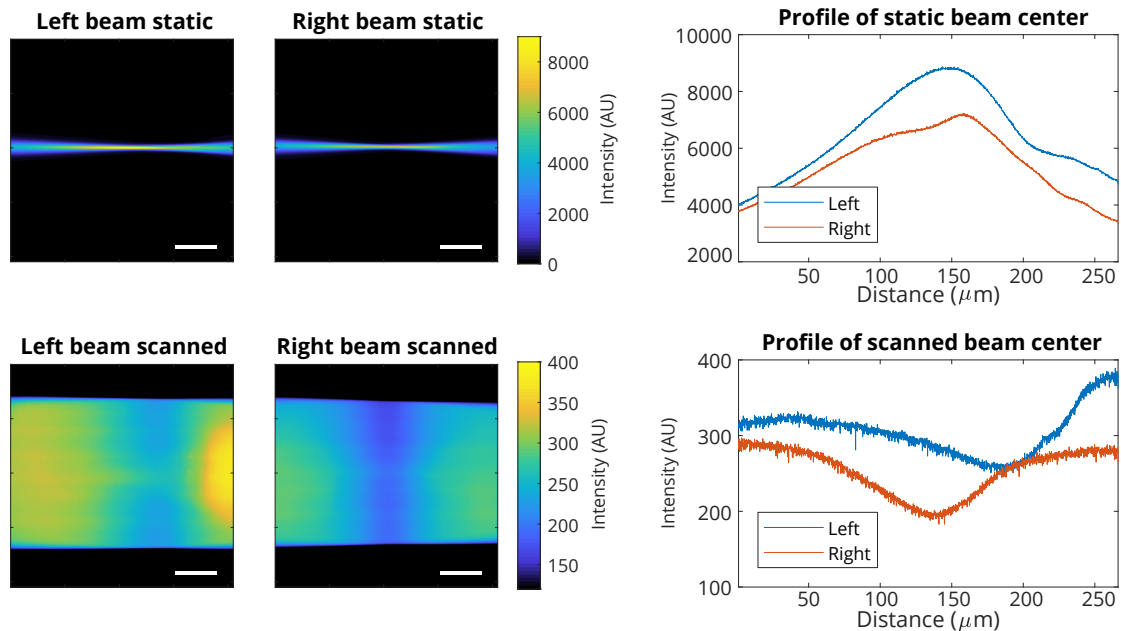


Figure 2.8: Illumination beam profile. Average of 50 stationary beam images for both left and right objectives (top left). Beam intensity profile along the center of each beam is plotted (top right). To simulate scanned beam illumination intensity, each beam image was averaged along the vertical axis (bottom left). Intensity profile of the projections are plotted (bottom right).

11 2.5.2 Resolution and point spread function measurement

12 To measure the resolution of the microscope, and characterize its optical perfor-
13 mance I performed point spread function measurement using fluorescently labeled beads
14 (TetraSpeck 500 nm, ThermoFisher). The beads were sonicated, and mixed with 0.8%
15 GelRite solution at a final dilution of 1:1000. The gel was loaded in glass capillaries and
16 allowed to cool. After the gel solidified, a ~1 mm piece was cut off and placed in the
17 microscope sample holder.

18 In order to establish an ideal, reference PSF, we simulated the theoretical PSF of the

1 microscope with the Gibson-Lanni model [95], using the MicroscPSF Matlab implemen-
 2 tation [96]. The advantage of this model is that it accounts for any differences between
 3 the experimental conditions and the design parameters of the objective, and thus it can
 4 simulate any possible aberrations that should arise. The adjustable parameters are the
 5 following (Fig. 2.9):

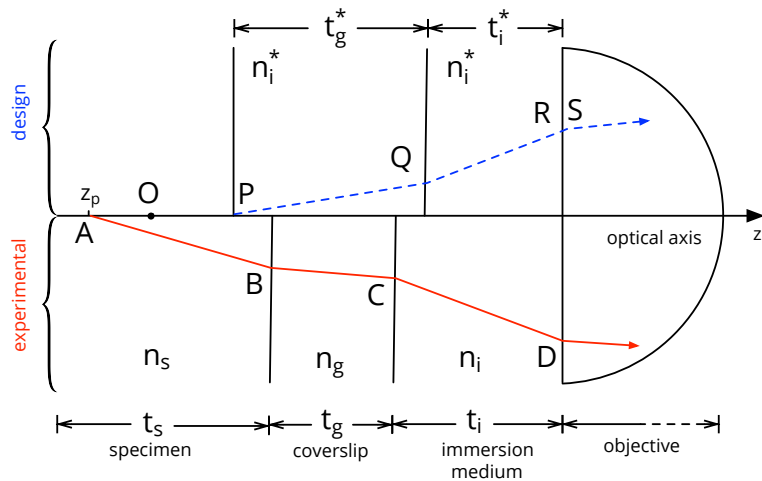


Figure 2.9: Schematics for the Gibson-Lanni model. The model is based on the differences in light propagation between the experimental (red) and design conditions (blue). The optical path length difference is calculated as follows: $OPD = [ABCD] - [PQRS]$. System properties are represented by vectors $\mathbf{n} = (n_i, n_i^*, n_g, n_g^*, n_s)$ and $\mathbf{t} = (t_i, t_i^*, t_g, t_g^*, t_s)$ for the refractive indices and path lengths respectively. Adapted from [96].

6 2.5.3 Stability of view switcher unit

2. DUAL MOUSE-SPIM

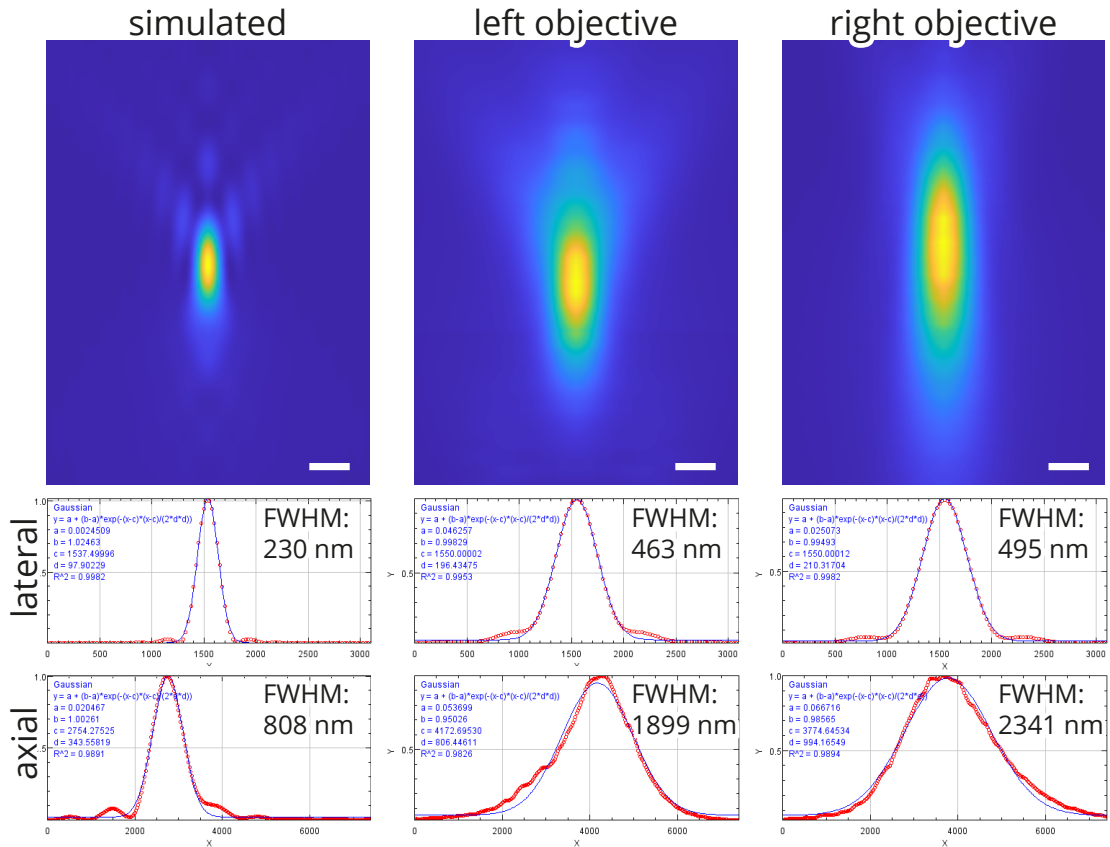


Figure 2.10: Simulated and measured PSF of Dual Mouse-SPIM. Top row: axial sections of simulated and measured point spread functions. Middle row: lateral intensity profile and Gaussian fit. Bottom row: Axial intensity profile and Gaussian fit. Simulations were performed based on the Gibson-Lanni model. Immersion medium and sample refractive index: 1.330, coverslip (FEP foil) refractive index: 1.344, coverslip distance: 1900 µm, coverslip thickness: 50 µm. Scale bar: 500 nm.

¹ Chapter 3

² Image processing for multi-view
³ microscopy

⁴ When using any kind of microscopy in research, image processing is a crucial part of the
⁵ workflow. This is especially true for light-sheet microscopy, since it's capable imaging the
⁶ same specimen for multiple days, producing immense amounts of data. A single overnight
⁷ experiment of *Drosophila* development (which is a very typical use-case for light-sheet)
⁸ can produce multiple terabytes of data. To see the real scales, let's consider the following
⁹ imaging conditions:

	camera	Hamamatsu Orca Flash 4
	image size	8 MB
¹⁰	1 stack = 250 planes	2 GB
	2 views	4 GB
	Time-lapse: 16 h @ 2/min	7.5 TB
	n colors	$n \cdot 7.5$ TB

¹¹ As it is apparent from this table,

3. IMAGE PROCESSING FOR MULTI-VIEW MICROSCOPY

1 3.1 Multi-view image fusion

2 3.1.1 Registration

3 Image based registration

4 Bead based registration

5 3.1.2 Transformation

6 Rigid

7 Affine

8 Elastic

9 3.1.3 Image fusion

10 Average

11 Sigmoidal weighted average

12 Fourier mixing

13 Huisken had something like this

14 Wavelet-based fusion

15 Multi-view deconvolution

16 [97] Uros thesis [98], [99] Spatially variant deconvolution

17 3.2 Image compression

18 Image compression is an important tool for everyday life, however it's rarely used in the
19 context of scientific imaging because of fear of information loss. This preconception is
20 mainly due to the famous blocking artifacts found in many highly compressed JPEG
21 images, however not all image compression algorithms introduce artifacts, and in fact
22 many lossless algorithms exist that would be suitable for such images. Nowadays, when
23 data production is in an exponential growth compression is again in highlight, without it
24 it would be extremely difficult to maintain many scientific projects that produce images
25 at a high data rate.

26 In this paper I will review the basics of image compression based on Sayood's text-
27 book, Introduction to Data Compression [100]. I will introduce some basics of information
28 theory and entropy, followed by discussing two widely used entropy coding algorithms,

1 Huffman coding and arithmetic coding. Section 3 will be about transform coding, specifically
 2 Discrete Cosine Transform (DCT) and wavelet transform while also touching upon
 3 techniques based on differential pulse code modulation. Finally I will show how some of
 4 the most widely used image compression standards use these methods to achieve effective
 5 image compression.

6 **3.2.1 Entropy coding**

7 **Information and Entropy**

8 "For the purpose of data compression it is useful to quantify the amount of *information*
 9 contained within a piece of data. The first rigorous definition of information was presented
 10 in an extremely influential paper by Shannon, published in two parts in 1948 [101, 102]."

11 "First, let's define the amount of self-information contained in the outcome of a
 12 random experiment:"

$$I(A) = \log_b \frac{1}{P(A)} = -\log_b P(A) \quad (3.1)$$

13 2 independent events:

$$P(A, B) = P(A) \cdot P(B) \quad (3.2)$$

self-information is additive:

$$I(A, B) = \log_b \frac{1}{P(A, B)} \quad (3.3)$$

$$= \log_b \frac{1}{P(A) \cdot P(B)} \quad (3.4)$$

$$= \log_b \frac{1}{P(A)} + \log_b \frac{1}{P(B)} \quad (3.5)$$

14 entropy for random variable X average or expected self-information for the random
 15 variable

$$H(X) = \sum_i P(A_i)I(A_i) = -\sum_i P(A_i) \log_b P(A_i) \quad (3.6)$$

16 entropy rate for data source S average information output by the data source

17 **Huffman coding**

18 Huffman coding is a prefix-free, optimal code that is widely used in data compression. It
 19 was developed by David A. Huffman as a course assignment on the first ever course on
 20 information theory at MIT, and was published shortly afterwards [103]. It is a variable
 21 length binary code which assigns different length codewords to letters of different prob-
 22 abilities. It is able to achieve optimal compression, which means the total length of the
 23 coded sequence will be minimal.

3. IMAGE PROCESSING FOR MULTI-VIEW MICROSCOPY

Table 3.1: Examples of a random binary code (#1) and a prefix-free binary code (#2). Code #2 is uniquely decodable, while for code #1 it's necessary to introduce boundaries between codewords to be able to distinguish them.

Letter	Code #1	Code #2
a_1	0	10
a_2	11	11
a_3	00	00
a_4	10	010
a_5	111	011

1 Although it produces a variable length code which can introduce some issues with
 2 decoding, it is still uniquely decodable. It achieves this property by using prefix-free
 3 codewords, meaning that none of the codewords are prefixes of any other codewords.
 4 This property can be exploited when decoding the codeword, since during this procedure
 5 the number of bits for the next codeword can not be determined in advance. However if
 6 no codeword is a prefix of another codeword, by simply reading the successive bits one
 7 by one until we reach a valid codeword, it's possible to uniquely decode the message.

8 Let's take the example in Table 3.2. Five letters are coded in binary code by Code
 9 #1 and by Code #2. Code 1 is not a prefix code, and because of this when reading the
 10 encoded sequence we can not be sure when we reach the end of a codeword. Decoding
 11 the sequence 0000 for example could be interpreted as 4 letters of a_1 or 2 letters of a_3 .

12 The Huffman coding procedure is based on two observations regarding optimal and
 13 prefix-free codes:

- 14 1. For a letter with higher frequency the code should produce shorter codewords, and
 15 for letters with lower frequency it should produce longer codewords.
 16 2. In an optimum code, the two least frequent codewords should have the same
 17 lengths.

18 From these statements the first is trivial to see that is correct. If the more frequent
 19 letters would have longer codewords than the less frequent letters, the average codeword
 20 length (weighted by the probabilities) would be larger than in the opposite case. Thus,
 21 more frequent letters must not have longer codewords than less frequent letter.

22 The second statement at first glance might not be so intuitive, so let's consider the
 23 following situation. The two least frequent codewords do not have the same lengths, that
 24 is the least frequent is longer. However, because this is a prefix code, the second longest
 25 codeword is not a prefix of the longest codeword. This means, if we truncate the longest
 26 codeword to the same length as the second longest, they will still be distinct codes and
 27 uniquely decodable. This way we have a new coding scheme which requires less space on
 28 average to code the same sequence as the original code, from which we can conclude the
 29 original code was not optimal. Therefore, for an optimal code, statement 2 must be true.

Table 3.2: Huffman code table.

Letter	Probability	Codeword
a_2	0.4	$c(a_2)$
a_1	0.2	$c(a_2)$
a_3	0.2	$c(a_2)$
a_4	0.1	$c(a_2)$
a_5	0.1	$c(a_2)$

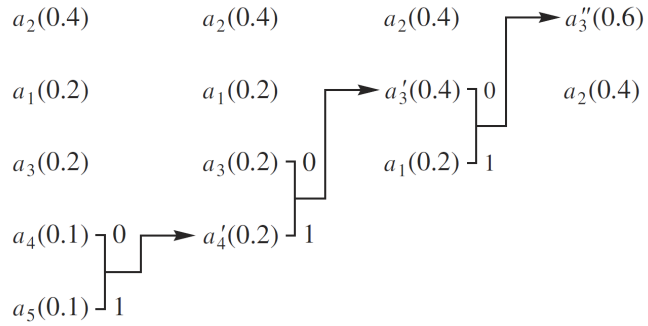


Figure 3.1: Building the binary Huffman tree. The letters are ordered by probability, these will be the final leave of the tree. To join the to branches at every iteration we join the to nodes with the smallest probability, and create a new common node with the sum of the probabilities. This process is continued until all nodes are joined in a root node with probability of 1. Now, if we traverse down the tree to each leaf, the codeword will be defined by their position.

To construct such a code, the following iterative procedure can be used. Let's consider an alphabet with five letters $A = [a_1, a_2, a_3, a_4, a_5]$ with $P(a_1) = P(a_3) = 0.2$, $P(a_2) = 0.4$ and $P(a_4) = P(a_5) = 0.1$ (Table 3.2). "The entropy for this source is 2.122 bits/symbol." Let's order the letters by probability, and consider the two least frequent. Since the codewords assigned to these should have the same lengths, "we can assign their codewords as"

$$\begin{aligned} c(a_4) &= \alpha_1 * 0 \\ c(a_5) &= \alpha_1 * 1 \end{aligned}$$

1 where $c(a_i)$ is the assigned codeword for letter a_i and $*$ denotes concatenation. Now
 2 we define a new alphabet A' with only four letters a_1, a_2, a_3, a'_4 , where a'_4 is a merged
 3 letter for a_4 and a_5 with the probability $P(a'_4) = P(a_4) + P(a_5) = 0.2$. We can continue
 4 this process of merging the letters until all of them are merged and we have only one letter
 5 left. Since this contains all of the original letters, its probability is 1. We can represent
 6 the end result in a binary tree (see Figure 3.1), where the leaves are the letter of the
 7 alphabet, nodes are the merged letters, and the codewords are represented by the path
 8 from the root node to each leaf (compare with Table 3.3). "The average length of this

3. IMAGE PROCESSING FOR MULTI-VIEW MICROSCOPY

Table 3.3: Huffman code table.

Letter	Probability	Codeword
a_2	0.4	1
a_1	0.2	01
a_3	0.2	000
a_4	0.1	0010
a_5	0.1	0011

1 code is”

$$l = 0.4 \times 1 + 0.2 \times 2 + 0.2 \times 3 + 0.1 \times 4 + 0.1 \times 4 = 2.2 \text{ bits/symbol} \quad (3.7)$$

2 ”A measure of the efficiency of this code is its redundancy—the difference between the
3 entropy and the average length. In this case, the redundancy is 0.078 bits/symbol. The
4 redundancy is zero when the probabilities are negative powers of two.”

5 Arithmetic coding

6 Although in this case the redundancy of the Huffman code is minimal, however in cases
7 where a few symbols have vary high probability compared to the rest, the redundancy
8 increases. This is simply because even for the most frequent letter the shortest codeword
9 the Huffman code can produce is of length 1.

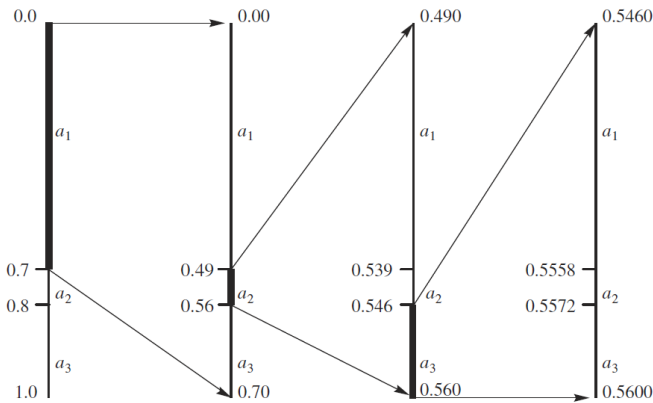
10 Let’s consider the following example: take alphabet $A = [a_1, a_2]$ with $P(a_1) = 0.95$
11 and $P(a_2) = 0.05$. The first order entropy for this source is $-0.95 \log 0.95 - 0.05 \log 0.05 =$
12 0.2864 bits/symbol, however if we assign the Huffman code we will have to use $c(a_1) = 0$
13 and $c(a_2) = 1$, which means the average length will be 1 bit/symbol. This means in order
14 to code this sequence using a Huffman code, we will need more than 3 times the number
15 of bits promised by the entropy.

16 To get around this fundamental limitation, a coding scheme must be used which does
17 not use discrete codewords at all. Arithmetic coding is the most well-known example of
18 such a scheme. The idea is due to Peter Elias. He developed it during the same course
19 on information theory in which Huffman developed his coding method, but he never
20 published it.

21 ”In order to distinguish a sequence of symbols from another sequence of symbols we
22 need to tag it with a unique identifier. One possible set of tags for representing sequences
23 of symbols are the numbers in the unit interval $[0,1]$. Because the number of numbers in
24 the unit interval is infinite, it should be possible to assign a unique tag to each distinct
25 sequence of symbols. In order to do this, we need a function that will map sequences of
26 symbols into the unit interval.”

Table 3.4: Example alphabet for arithmetic coding.

Letter	Probability
a_1	0.7
a_2	0.1
a_3	0.2


 Figure 3.2: Arithmetic coding scheme in practice with the alphabet from Table 3.4 on the sequence a_1, a_2, a_3 .

1 ”A straightforward algorithm to arithmetically encode a given input string is the
 2 following: Partition the unit interval $[0, 1)$ into sub-intervals and assign one subinterval
 3 to each symbol in the input alphabet. The sizes of the sub-intervals are chosen to be
 4 proportional to the symbol frequencies. A string of symbols can be encoded by applying
 5 this process recursively: The sub-interval from the previous step is subdivided again
 6 using the same proportions. Figure 3.2. shows an example of arithmetic coding using the
 7 symbol frequencies given in Table 3.4.”

8 This kind of coding although easy to understand, it’s actually quite cumbersome to
 9 directly implement on a computer, where only a certain floating point precision can be
 10 achieved. For real life use this precision is often unsatisfactory, so some extra steps are
 11 involved in the coding.

12 Since after each step the next subinterval is a subset of the previous interval, if the
 13 coding interval after a certain number of steps is contained in either the upper or lower
 14 half of the unit interval it will remain there for the rest of the coding. We can exploit
 15 this fact by rescaling that interval to the unit interval and writing either a 0 or 1 bit to
 16 the output depending on the position of the subinterval. By continuing this scheme it’s
 17 possible to reach arbitrary precision even using a computer.

18 The decoding process is analogous to encoding. The decoder keeps track of the current
 19 lower and upper bounds. It mimics the rescaling operations of the encoder based on the
 20 bits of the encoded binary number.

3. IMAGE PROCESSING FOR MULTI-VIEW MICROSCOPY

1 3.2.2 Transform coding

2 The methods outlined in the previous section are effective at compressing the data in an
3 optimal way and reaching the first order entropy, however they assume nothing about the
4 structure of the data. For image compression it's important to also consider this, since
5 most images have a relatively high level of autocorrelation, meaning that neighboring
6 values have a high chance of being similar, although not necessarily equal. Transform
7 coding is a technique that by itself does not compress the data, however by exploiting
8 some knowledge of the structure it transforms the data effectively reducing its first or-
9 der entropy. When regular entropy coding is then performed on the transformed data,
10 because of the reduced first-order entropy, these techniques can achieve a higher rate
11 of compression. At decompression, after decoding the entropy coder, the reverse trans-
12 formation is applied to reveal the original data. This section will introduce two of the
13 most important algorithms for transform coding, Discrete Cosine Transform and Discrete
14 Wavelet Transform.

15 **Discrete Cosine Transform**

16 Discrete Cosine Transform [104] is closely related to the well known Fourier transform.
17 The main idea behind this is to represent a function by a weighted sum of different sine
18 and cosine functions. This provides a different view, instead of looking at the data in the
19 time domain, we gain information about the frequencies that compose the signal.

20 "Discrete Cosine Transform is a variant of the discrete Fourier transformation", how-
21 ever instead of making the signal periodic which can introduce large jumps at the edges,
22 the signal is extended in a symmetric way. Since this will give a smooth transition even at
23 the boundaries, the transform does not have to include so many high frequency compo-
24 nents. Also, because of the symmetric extension, it's possible to represent the functions
25 only by using the cosine bases, resulting in fewer coefficients. Overall, the DCT is much
26 better suited for compression, than DFT.

27 The DCT base functions are defined in the following way:

$$c_{i,j} = s_i \cdot \cos \frac{(2j+1)i\pi}{2n} \quad \text{with } s_i = \begin{cases} \sqrt{\frac{1}{n}} & \text{if } i = 0 \\ \sqrt{\frac{2}{n}} & \text{otherwise} \end{cases} \quad (3.8)$$

28 "The scaling factors are chosen so that the L_2 norm of each basis vector is 1 and so
29 the transform is orthonormal. The inverse transform can therefore be found by simply
30 transposing the transform matrix."

31 Applying the DCT to two dimensional functions, i.e. images is very similar to the
32 two dimensional Fourier transform. The base functions are the outer products of the 1D
33 base functions (Figure 3.3.), and the transform can actually be performed separately for

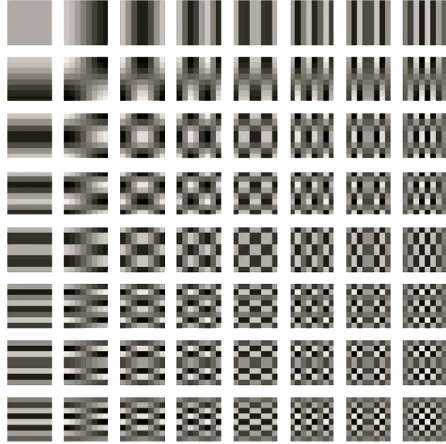


Figure 3.3: Basis functions of the 8×8 2D DCT, computed as the outer product of the 1D basis vectors..

1 each dimension.

2 Computation effort in a naive implementation is $O(n^2)$ but since DCT is based on the
 3 Fourier transform, an $O(n \log n)$ algorithm is also possible, analogous to the fast Fourier
 4 transform. This is still larger than a linear scaling with the data size, which can be very
 5 inconvenient. Therefore, in practice the DCT is usually applied to smaller blocks of the
 6 image, such as 4×4 , 8 or 16×16 .

7 Although DCT is an effective way of reducing the first-order entropy, it has a potential
 8 shortcoming by its use of floating point arithmetic. Because of the finite machine precision
 9 inherent rounding errors will occur, which means the reverse transformation can not
 10 generate the exact original data. For many application, such as photography, this still can
 11 be acceptable, but for scientific image data lossy compression is generally not accepted.

12 DCT-like integer-based variants in JPEG-XR, and H.264

13 Discrete Wavelet Transform

14 ”!!CHANGE THIS!!Methods based on Fourier analysis, such as the DCT introduced in
 15 the previous section, give excellent localization in frequency space: They tell us exactly
 16 which frequencies occur in the data, which is very useful for data compression. However,
 17 they give no spatial localization: They do not tell us where in the signal these frequencies
 18 occur. Every DCT base function affect the whole image domain!!UNTIL HERE!!”, which
 19 means distinct local structures can have a global effect on the final outcome. In case of
 20 an edge for example, it’s necessary to include a high frequency component with a large
 21 coefficient, but since every DCT base function has an impact on the whole domain, this
 22 will have to be compensated on smoother regions by also increasing the coefficients of
 23 other factors. This can negatively impact compression performance.

24 A solution for this is to use different base functions, namely ones with finite support.

3. IMAGE PROCESSING FOR MULTI-VIEW MICROSCOPY

¹ This way we will not only be able to get information about the frequency, but also about
² the localization of that frequency in some extent.

³ ”!!!!One option for such a set of local basis functions, and certainly the most popular one, is the multi-resolution analysis based on wavelets. The term “multi-resolution analysis” in the context of wavelets was introduced in the late 1980s by Stéphane Mallat [105], though research on wavelets had been ongoing for several years before that.!!!!”

⁷ ”The idea behind the wavelet multi-resolution analysis is to build a basis out of
⁸ translated and scaled versions of one underlying function called the *mother wavelet* ψ .
⁹ The mother wavelet is non-zero only in a small region, leading to the locality properties.
¹⁰ It is translated to cover the whole domain. It also covers only a small frequency band,
¹¹ and is scaled to cover higher or lower frequencies. The family of translated and scaled
¹² functions $\psi_{l,i}$ is generated from according to”

$$\psi_{l,i}(t) = \sqrt{2^l} \psi(2^l t - i), \quad l, i \in \mathbb{Z} \quad (3.9)$$

¹³ ”Incrementing l halves the width of the resulting function, which thus corresponds to
¹⁴ a higher frequency band. Changing i moves the function along the x axis. The size of
¹⁵ each step scales with the width of the function, defined by l . The normalization factor
¹⁶ $\sqrt{2^l}$ is chosen so that the L_2 norm stays constant. The mother wavelet can be chosen
¹⁷ so that the $\psi_{l,i}$ are pairwise orthogonal and thus form a basis of some function space.
¹⁸ However, representing a function in this basis will generally require an infinite number
¹⁹ of basis functions $\psi_{l,i}$: To represent a constant component, i.e. content of frequency zero,
²⁰ the wavelet must be infinitely scaled. To address this, it is necessary to introduce an
²¹ additional scaling function ϕ which complements the wavelet. It is scaled and translated
²² the same way as the mother wavelet.”

²³ The oldest wavelets are the Haar wavelets, and because of their simplicity, they
²⁴ provide a good example on how wavelet transformation works. The Haar wavelet scaling
²⁵ ϕ and wavelet ψ functions are the following:

$$\phi(t) = \begin{cases} 1 & \text{if } 0 \leq t < 1 \\ 0 & \text{otherwise} \end{cases} \quad (3.10)$$

$$\psi(t) = \begin{cases} -1 & \text{if } 0 \leq t < \frac{1}{2} \\ 1 & \text{if } \frac{1}{2} \leq t < 1 \\ 0 & \text{otherwise} \end{cases} \quad (3.11)$$

²⁶ ”Clearly, all wavelet functions $\psi_{l,i}$ are orthogonal. Additionally, the scaling functions $\phi_{l,i}$
²⁷ at a fixed level i are orthogonal. The scaling functions $\phi_{l,i}$ are also orthogonal to the
²⁸ wavelet functions $\psi_{k,i}$, $k \geq l$ at the same and all finer levels.”

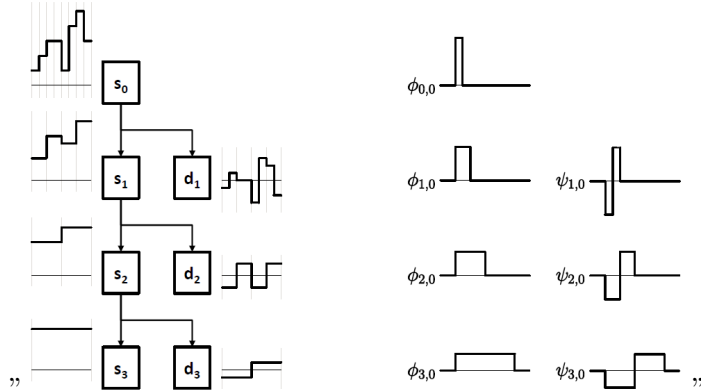


Figure 3.4: Multi-resolution wavelet decomposition, using the Haar wavelets as an example. Left: decomposition to multiple levels of low pass and high pass coefficients corresponding to the scaling and the wavelet functions respectively. Right: some of the base wavelet functions used for the decomposition.

1 "Figure 3.4. (left) schematically shows the decomposition of a signal into low-pass
 2 components corresponding to the scaling function, and high-pass components correspond-
 3 ing to the wavelet. The signal s_0 can be represented by the translated scaling function
 4 at a finer scale l_0 , which can be decomposed to the sum of a coarser approximation
 5 s_1 corresponding to the scaling function and the detail part d_1 corresponding to the
 6 wavelet functions. This decomposition to a sum of coarser approximation and detail can
 7 be continued multiple times, thus resulting in the previously mentioned multi-resolution
 8 analysis.

9 Of course, for image compression applications, it is desirable to extend this trans-
 10 formation to a 2D version, that can be applied to the images before performing the
 11 arithmetic coding. Similarly to the DCT, the wavelet transform is also separable, and
 12 can be performed as a sequence of 1D transforms along different directions. Separable in
 13 a sense, that it does not matter in which order the individual 1D DWTs are applied to
 14 get the same 2D transformation.

15 JPEG [106], JPEG-LS [107] and JPEG2000

3. IMAGE PROCESSING FOR MULTI-VIEW MICROSCOPY

¹ **3.2.3 Differential pulse code modulation / LOCO-I?**

² **3.3 Noise in light microscopy images**

³ **3.3.1 Photon shot noise**

⁴ **3.3.2 Camera noise**

⁵ **CCD**

⁶ **EM-CCD**

⁷ **sCMOS**

⁸ **3.3.3 Variance stabilization**

¹ Chapter 4

² Real-time, GPU accelerated
³ image processing pipeline

⁴ 4.1 GPU architecture

⁵ 4.2 Live fusion

⁶ 4.2.1 MuVi-SPIM

⁷ 4.2.2 Bead based registration

⁸ 4.3 B³D image compression

⁹ B³D image compression B³D image compression

¹⁰ 4.3.1 Data sizes in microscopy

¹¹ 4.3.2 Lossless compression performance

¹² 4.3.3 Benchmarking

¹³ 4.4 Noise dependent lossy compression

¹⁴ 4.5 Methods

4. REAL-TIME, GPU ACCELERATED IMAGE PROCESSING PIPELINE

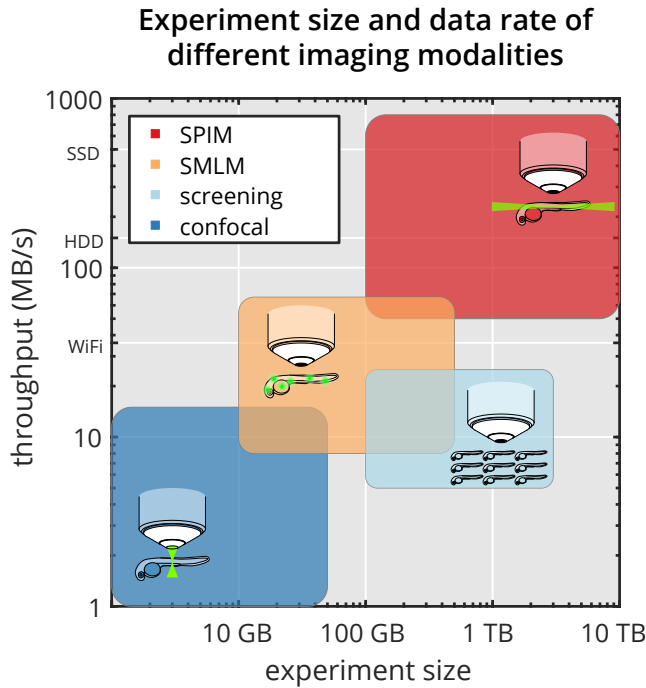


Figure 4.1: Experiment sizes and data rate of different imaging modalities.. Comparison of single-plane illumination microscopy (SPIM, red rectangle), high-content screening (light blue), single molecule localization microscopy (SMLM, orange) and confocal microscopy (blue) by typical experiment size and data production rate (see also Table 4.1).

imaging device	image size	frame rate	data rate	data size
SPIM	2048x2048	50/s	800 MB/s	10 TB
SMLM	512x512	56/s	56 MB/s	500 GB
screening	1344x1024	8.5s/	22 MB/s	5 TB
confocal	512x512	5/s	12.5 MB/s	50 GB

Table 4.1: Data sizes in microscopy. Typical devices used for confocal microscopy, high-content screening, single-molecule localization microscopy and light-sheet microscopy and their data production characteristics. Data visualized on Figure 4.1

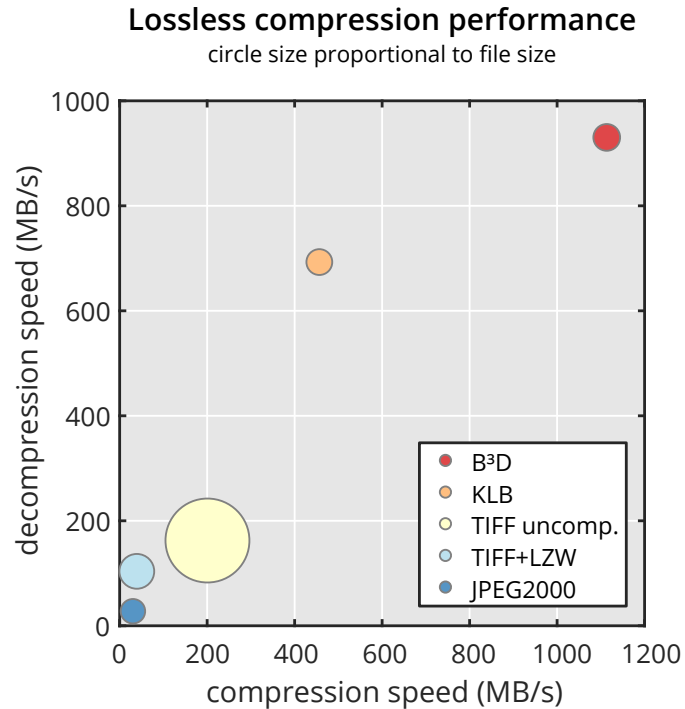


Figure 4.2: Lossless compression performance. Performance comparison of our B³D B³D compression algorithm (red circle) vs. KLB (orange), uncompressed TIFF (light yellow), LZW compressed TIFF (light blue) and JPEG2000 (blue) regarding write speed (horizontal axis), read speed (vertical axis) and file size (circle size). (see also Table 4.2).

	write speed	read speed	CR	file size
B³D	1,115.08 MB/s	928.97 MB/s	9.861	100%
KLB	283.19 MB/s	619.95 MB/s	10.571	93.28%
JPEG2000	31.94 MB/s	26.38 MB/s	11.782	83.69%
JPEG2000	202.32 MB/s	161.08 MB/s	1.00	986.1%
TIFF + LZW	40.85 MB/s	102.37 MB/s	5.822	169.37%

Table 4.2: Lossless compression performance. B³D is compared with various popular lossless image compression methods regarding write speed, read speed and compression ratio (original size / compressed size). Data visualized on Figure 4.2.

4. REAL-TIME, GPU ACCELERATED IMAGE PROCESSING PIPELINE

Dataset name	Imaging modality	Description	Size (MB)
drosophila	SPIM	dataset acquired in MuVi-SPIM of a Drosophila melanogaster embryo expressing H2Av-mCherry nuclear marker	494.53
zebrafish	SPIM	dataset acquired in MuVi-SPIM of a zebrafish embryo expressing b-actin::GCaMP6f calcium sensor	2,408.00
phallusia	SPIM	dataset acquired in MuVi-SPIM of a Phallusia mammillata embryo expressing PH-citrine membrane marker	1,323.88
simulation	SMLM	MT0.N1.LD-2D simulated dataset of microtubules labeled with Alexa Fluor 647 from SMLMS 2016 challenge	156.22
microtubules	SMLM	microtubules immuno-labeled with Alexa Fluor 674-bound antibodies in U2OS cells	1,643.86
lifeact	SMLM	actin network labeled with LifeAct-tdEOS in U2OS cells	3,316.15
dapi	screening	wide field fluorescence images of DAPI stained HeLa Kyoto cells [108]	1,005.38
vsvg	screening	wide field fluorescence images of CFP-tsO45G proteins in HeLa Kyoto cells [108]	1,005.38
membrane	screening	wide field fluorescence images of membrane localized CFP-tsO45G proteins labeled with AlexaFluor647 in HeLa Kyoto cells [108]	1,005.38

Table 4.3: Datasets used for benchmarking compression performance.

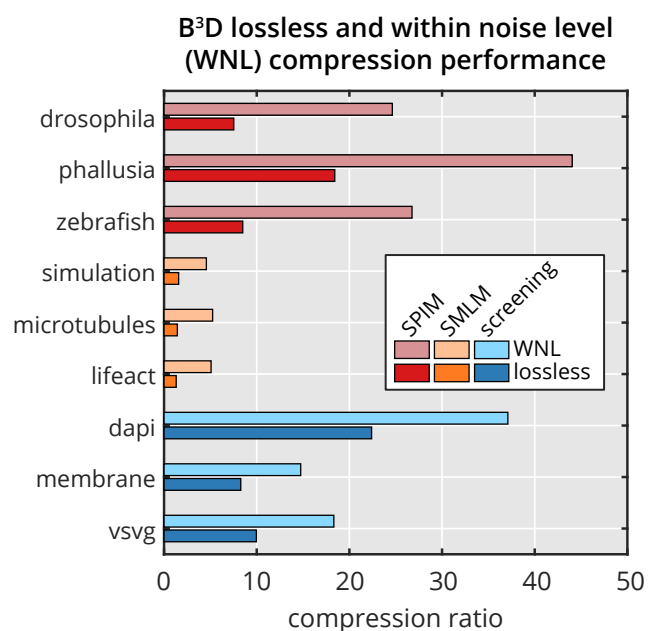


Figure 4.3: Within noise level compression performance.. For description of datasets see Table 4.3.

4. REAL-TIME, GPU ACCELERATED IMAGE PROCESSING PIPELINE

¹ Chapter 5

² Discussion

³ 5.1 New scientific results

⁴ **Thesis I.** *I have designed and constructed a new light-sheet microscope suitable for*
⁵ *high sensitivity imaging of delicate samples. A novel arrangement of two high numerical*
⁶ *aperture objectives in 120 degrees allows for near isotropic resolution while increasing*
⁷ *light collection efficiency by a factor of two.*

⁸ Corresponding publications: [J3], [J2], [J1]

⁹ Live imaging of light sensitive specimens, such as a developing mouse embryo is a chal-
¹⁰ lenging task

¹¹ **Thesis II.** *I have developed a GPU-based image processing pipeline for multi-view light-*
¹² *sheet microscopy that enables real time fusion of opposing views.*

¹³ Corresponding publications: [C1], [C2], [C3]

¹⁴ **Thesis III.** *I have developed a new image compression algorithm that enables noise*
¹⁵ *dependent lossy compression of light microscopy images, and can reach a compression*
¹⁶ *ratio of 100 fold while preserving the results of downstream data analysis steps.*

¹⁷ Corresponding publications: [J4], [C1], [C2], [C3]

¹⁸ All microscopy images contain inherent noise, that is

¹⁹ **Thesis IV.** *I have developed a new GPU-based image compression library, B^3D , that*
²⁰ *implements the algorithm described in Thesis III, and allows for real time compression*
²¹ *of microscopy images with a throughput of up to 1 GB/s.*

²² Corresponding publications: [J4], [C1], [C2], [C3]

²³ B^3D is an efficient, GPU-based image compression library allowing lossless and noise
²⁴ dependent lossy compression of microscopy images. Since many high-speed microscopy

5. DISCUSSION

- ¹ methods generate immense amounts of data, easily reaching terabytes per experiment,
- ² image compression is especially important to efficiently deal with such datasets.

¹ Acknowledgements

ACKNOWLEDGEMENTS

¹ Appendix A

² Bill of Materials

³ Optical components

⁴ • Lenses

- ⁵ – 2×Nikon CFI75 Apo LWD 25x/1.10w water dipping objectives
- ⁶ – 2×Nikon ITL200 200 mm tube lens
- ⁷ – 2×200 mm x 25 mm Dia. achromatic lens (Edmunds Optics, #47-645)
- ⁸ – 2×400 mm x 40 mm Dia. achromatic lens (Edmunds Optics, #49-281)
- ⁹ – 2×75 mm x 25 mm Dia. achromatic lens (Edmunds Optics, #47-639)

¹⁰ • Filters

- ¹¹ – 2×BrightLine quad-edge dichroic beam splitter (Semrock, Di03-R405/488/561/635-t3-25x36)
- ¹² – EdgeBasic 488 nm long pass filter (Semrock, BLP01-488R-25)
- ¹³ – BrightLine 525/50 band pass filter (Semrock, FF03-525/50-25)
- ¹⁴ – EdgeBasic 561 nm long pass filter (Semrock, BLP02-561R-25)
- ¹⁵ – RazorEdge 647 nm long pass filter (Semrock, LP02-647RU-25)

¹⁷ • Mirrors

- ¹⁸ – 6×1” Broadband Dielectric Elliptical Mirror (Thorlabs, BBE1-E03)
- ¹⁹ – 2×30 mm Broadband 1/10λ Mirror (OptoSigma, TFMS-30C05-4/11)
- ²⁰ – 10 Pack of 1” Protected Silver Mirrors (Thorlabs, PF10-03-P01-10)
- ²¹ – Knife-Edge Right-Angle Prism Dielectric Mirror (Thorlabs, MRAK25-E02)

²² Mechanical components

- ²³ • 40 mm travel range pneumatic cylinder (Airtac, HM-10-040)
- ²⁴ • 5/2-way electric valve (Airtac, M-20-510-HN)
- ²⁵ • 2×25 mm extended contact bearing steel stage (OptoSigma, TSDH-251C)
- ²⁶ • 30x90 mm stainless steel slide (OptoSigma, IPWS-F3090)
- ²⁷ • close proximity gimbal mirror mount (Thorlabs, GMB1/M)
- ²⁸ • 30 mm cage elliptical mirror mount (Thorlabs, KCB1E)

²⁹ Custom parts

- ³⁰ All parts are (anodized) aluminium, unless stated otherwise.

APPENDIX A

- 1 • 2×mirror holder block
- 2 • Front plate for objective, chamber and mirror mounting
- 3 • Imaging chamber (PEEK)
- 4 • Wedge ring and matching threads to fasten objectives
- 5 • Camera bridge
- 6 • Illumination splitter unit
- 7 • adapter plates to mount stages

8 Electronics

- 9 • Embedded system (National Instruments, cRIO-9068) equipped with:
 - 10 – 2×C series digital I/O card (NI 9401)
 - 11 – 1×C Series 100 kS/s 4-channel Voltage Output Module (NI 9263)
 - 12 – 1×C Series 25 kS/s 16-channel Voltage Output Module (NI 9264)
- 13 • Omicron SOLE-3 laser combiner, with 488, 561 and 638 nm laser lines
- 14 • Andor Zyla 4.2 sCMOS Camera
- 15 • Galvanometric scanner mirror (Cambridge Technology, 6210B)
- 16 • 6 position filter wheel (Ludl Electronic Products, 96A361)
- 17 • Filter wheel controller unit (Ludl Electronic Products, MAC5000)
- 18 • 2 piezoelectric stages (Nanos Instruments, LPS-30-30-1-V2_61-S-N)
- 19 • 2 stage controller boards (Nanos Instruments, BMC101)

¹ References

² The author's publications

- ³ [J1] Patrick Hoyer et al. "Breaking the diffraction limit of light-sheet fluorescence mi-
⁴ croscopy by RESOLFT". *Proceedings of the National Academy of Sciences* 113.13
⁵ (Mar. 2016), pp. 3442–3446. DOI: [10.1073/pnas.1522292113](https://doi.org/10.1073/pnas.1522292113) (cit. on pp. 16, 17,
⁶ 59).
- ⁷ [J2] Petr Strnad et al. "Inverted light-sheet microscope for imaging mouse pre-
⁸ implantation development". *Nature Methods* 13.2 (Feb. 2016), pp. 139–142. DOI:
⁹ [10.1038/nmeth.3690](https://doi.org/10.1038/nmeth.3690) (cit. on pp. 16, 23, 24, 29, 59).
- ¹⁰ [J3] Gustavo de Medeiros, Bálint Balázs, and Lars Hufnagel. "Light-sheet imaging
¹¹ of mammalian development". *Seminars in Cell & Developmental Biology. Mammalian*
¹² development 55 (July 2016), pp. 148–155. DOI: [10.1016/j.semcdb.2015.11.001](https://doi.org/10.1016/j.semcdb.2015.11.001) (cit. on pp. 16, 59).
- ¹⁴ [J4] Balint Balazs, Joran Deschamps, Marvin Albert, Jonas Ries, and Lars Hufnagel.
¹⁵ "A real-time compression library for microscopy images". *bioRxiv* (July 2017),
¹⁶ p. 164624. DOI: [10.1101/164624](https://doi.org/10.1101/164624) (cit. on p. 59).

¹⁷ The author's others publications

- ¹⁸ [J5] Zoltán Jakus, Edina Simon, Bálint Balázs, and Attila Mócsai. "Genetic deficiency
¹⁹ of Syk protects mice from autoantibody-induced arthritis". *Arthritis and Rheumatism* 62.7
²⁰ (July 2010), pp. 1899–1910. DOI: [10.1002/art.27438](https://doi.org/10.1002/art.27438).
- ²¹ [J6] Balázs Győrffy et al. "RecurrenceOnline: an online analysis tool to determine
²² breast cancer recurrence and hormone receptor status using microarray data".
²³ *Breast Cancer Research and Treatment* (July 2011). DOI: [10.1007/s10549-011-1676-y](https://doi.org/10.1007/s10549-011-1676-y).

References cited in the thesis

- 1 [J7] Weiwei Shi et al. “Combined analysis of gene expression, DNA copy number, and
2 mutation profiling data to display biological process anomalies in individual breast
3 cancers”. *Breast Cancer Research and Treatment* 144.3 (Mar. 2014), pp. 561–568.
4 DOI: 10.1007/s10549-014-2904-z.

5 The author’s conference presentations

- 6 [C1] Bálint Balázs, Marvin Albert, and Lars Hufnagel. “GPU-based image processing
7 for multiview microscopy data”. *Light Sheet Fluorescence Microscopy Interna-*
8 *tional Conference*. Sheffield, UK, Sept. 2016 (cit. on p. 59).
9 [C2] Bálint Balázs, Marvin Albert, and Lars Hufnagel. “GPU-based image processing
10 for multi-view microscopy data”. *Focus on Microscopy*. Taipei, Taiwan, Mar. 2016
11 (cit. on p. 59).
12 [C3] Bálint Balázs, Marvin Albert, and Lars Hufnagel. “GPU-based image processing
13 for multi-view microscopy data”. *Focus on Microscopy*. Bordeaux, France, Apr.
14 2017 (cit. on p. 59).

15 References cited in the thesis

- 16 [1] Scott F. Gilbert. *Developmental Biology*. 10th. Sinauer Associates, 2013 (cit. on
17 p. 3).
18 [2] Alberto Diaspro. *Optical Fluorescence Microscopy: From the Spectral to the Nano*
19 *Dimension*. 1st ed. Springer-Verlag Berlin Heidelberg, 2011 (cit. on pp. 3, 4).
20 [3] Uros Krzic, Stefan Gunther, Timothy E. Saunders, Sebastian J. Streichan, and
21 Lars Hufnagel. “Multiview light-sheet microscope for rapid *in toto* imaging”. *Nature*
22 *Methods* 9.7 (July 2012). MuVi-SPIM, pp. 730–733. DOI: 10.1038/nmeth.2064 (cit. on pp. 3, 16, 17).
23 [4] Raju Tomer, Khaled Khairy, Fernando Amat, and Philipp J. Keller. “Quantitative
24 high-speed imaging of entire developing embryos with simultaneous multiview
25 light-sheet microscopy”. *Nature Methods* 9.7 (July 2012). SimView, pp. 755–763.
26 DOI: 10.1038/nmeth.2062 (cit. on pp. 3, 16, 17).
27 [5] Hans-Ulrich Dodt et al. “Ultramicroscopy: three-dimensional visualization of neu-
28 ronal networks in the whole mouse brain”. *Nature Methods* 4.4 (Mar. 2007),
29 pp. 331–336. DOI: 10.1038/nmeth1036 (cit. on pp. 3, 16, 27).
30

- 1 [6] Bi-Chang Chen et al. “Lattice light-sheet microscopy: Imaging molecules to
2 embryos at high spatiotemporal resolution”. *Science* 346.6208 (Oct. 2014),
3 p. 1257998. DOI: 10.1126/science.1257998 (cit. on pp. 3, 17, 37).
- 4 [7] P. Philippe Laissie, Rana A. Alghamdi, Pavel Tomancak, Emmanuel G. Reynaud,
5 and Hari Shroff. “Assessing phototoxicity in live fluorescence imaging”. *Nature
Methods* 14.7 (July 2017), pp. 657–661. DOI: 10.1038/nmeth.4344 (cit. on pp. 3,
6 4).
- 8 [8] Jeff W. Lichtman and José-Angel Conchello. “Fluorescence microscopy”. *Nature
Methods* 2.12 (Dec. 2005), pp. 910–919. DOI: 10.1038/nmeth817 (cit. on p. 4).
- 10 [9] G. G. Stokes. “On the Change of Refrangibility of Light”. *Philosophical Transactions
of the Royal Society of London* 142 (Jan. 1852), pp. 463–562. DOI: 10.1098/
rstl.1852.0022 (cit. on p. 4).
- 13 [10] *Spectra Viewer*. URL: <https://www.chroma.com/spectra-viewer> (visited on
14 09/11/2017) (cit. on p. 5).
- 15 [11] Robert Bacallao, Morgane Bomsel, Ernst H. K. Stelzer, and Jan De Mey. “Guiding
16 Principles of Specimen Preservation for Confocal Fluorescence Microscopy”. *Hand-
17 book of Biological Confocal Microscopy*. DOI: 10.1007/978-1-4615-7133-9_18.
18 Springer, Boston, MA, 1990, pp. 197–205 (cit. on p. 5).
- 19 [12] O. Shimomura, F. H. Johnson, and Y. Saiga. “Extraction, purification and prop-
20 erties of aequorin, a bioluminescent protein from the luminous hydromedusan,
21 Aequorea”. *Journal of Cellular and Comparative Physiology* 59 (June 1962). first
22 purification of GFP from jellyfish, pp. 223–239 (cit. on p. 5).
- 23 [13] Douglas C. Prasher, Virginia K. Eckenrode, William W. Ward, Frank G. Prender-
24 gast, and Milton J. Cormier. “Primary structure of the Aequorea victoria green-
25 fluorescent protein”. *Gene* 111.2 (Feb. 1992). cloning GFP cDNA, pp. 229–233.
26 DOI: 10.1016/0378-1119(92)90691-H (cit. on p. 5).
- 27 [14] M. Chalfie, Y. Tu, G. Euskirchen, W. W. Ward, and D. C. Prasher. “Green
28 fluorescent protein as a marker for gene expression”. *Science* 263.5148 (Feb. 1994).
29 GFP in c. elegans / nematodes, pp. 802–805. DOI: 10.1126/science.8303295
30 (cit. on p. 5).
- 31 [15] Adam Amsterdam, Shuo Lin, and Nancy Hopkins. “The Aequorea victoria Green
32 Fluorescent Protein Can Be Used as a Reporter in Live Zebrafish Embryos”. *De-
33 velopmental Biology* 171.1 (Sept. 1995). first GFP zebrafish, pp. 123–129. DOI:
34 10.1006/dbio.1995.1265 (cit. on p. 5).

References cited in the thesis

- [16] Masaru Okabe, Masahito Ikawa, Katsuya Kominami, Tomoko Nakanishi, and Yoshitake Nishimune. “‘Green mice’ as a source of ubiquitous green cells”. *FEBS Letters* 407.3 (May 1997). first EGFP mouse, pp. 313–319. DOI: 10.1016/S0014-5793(97)00313-X (cit. on p. 5).
- [17] R Heim, D C Prasher, and R Y Tsien. “Wavelength mutations and posttranslational autoxidation of green fluorescent protein.” *Proceedings of the National Academy of Sciences of the United States of America* 91.26 (Dec. 1994), pp. 12501–12504 (cit. on p. 5).
- [18] Roger Heim and Roger Y Tsien. “Engineering green fluorescent protein for improved brightness, longer wavelengths and fluorescence resonance energy transfer”. *Current Biology* 6.2 (Feb. 1996), pp. 178–182. DOI: 10.1016/S0960-9822(02)00450-5 (cit. on p. 5).
- [19] Brendan P. Cormack, Raphael H. Valdivia, and Stanley Falkow. “FACS-optimized mutants of the green fluorescent protein (GFP)”. *Gene. Flourescent Proteins and Applications* 173.1 (1996), pp. 33–38. DOI: 10.1016/0378-1119(95)00685-0 (cit. on p. 5).
- [20] Robert F. Service. “Three Scientists Bask in Prize’s Fluorescent Glow”. *Science* 322.5900 (Oct. 2008), pp. 361–361. DOI: 10.1126/science.322.5900.361 (cit. on p. 5).
- [21] E. Abbe. “Beiträge zur Theorie des Mikroskops und der mikroskopischen Wahrnehmung”. *Archiv für mikroskopische Anatomie* 9.1 (1873), pp. 413–418. DOI: 10.1007/BF02956173 (cit. on p. 7).
- [22] Max Born and Emil Wolf. *Principles of Optics: Electromagnetic Theory of Propagation, Interference and Diffraction of Light*. Elsevier, June 2013 (cit. on pp. 8, 9).
- [23] C. J. R. Sheppard and H. J. Matthews. “Imaging in high-aperture optical systems”. *JOSA A* 4.8 (Aug. 1987), pp. 1354–1360. DOI: 10.1364/JOSAA.4.001354 (cit. on p. 8).
- [24] Lord Rayleigh F.R.S. “XXXI. Investigations in optics, with special reference to the spectroscope”. *Philosophical Magazine* 8.49 (Oct. 1879), pp. 261–274. DOI: 10.1080/14786447908639684 (cit. on p. 9).
- [25] Jim Swoger, Jan Huisken, and Ernst H. K. Stelzer. “Multiple imaging axis microscopy improves resolution for thick-sample applications”. *Optics Letters* 28.18 (Sept. 2003), p. 1654. DOI: 10.1364/OL.28.001654 (cit. on p. 11).

- 1 [26] Jim Swoger, Peter Verveer, Klaus Greger, Jan Huisken, and Ernst H. K. Stelzer.
2 “Multi-view image fusion improves resolution in three-dimensional microscopy”.
3 *Optics Express* 15.13 (2007), p. 8029. DOI: 10.1364/OE.15.008029 (cit. on p. 11).
- 4 [27] Marvin Minsky. “Microscopy apparatus”. US3013467 A. U.S. Classification
5 356/432, 359/389, 348/79, 250/215; International Classification G02B21/00;
6 Cooperative Classification G02B21/0024, G02B21/002; European Classification
7 G02B21/00M4A, G02B21/00M4. Dec. 1961 (cit. on p. 12).
- 8 [28] Paul Davidovits and M. David Egger. “Scanning Laser Microscope”. *Nature*
9 223.5208 (Aug. 1969), pp. 831–831. DOI: 10.1038/223831a0 (cit. on p. 12).
- 10 [29] Ernst H.K. Stelzer and Steffen Lindek. “Fundamental reduction of the observation
11 volume in far-field light microscopy by detection orthogonal to the illumination
12 axis: confocal theta microscopy”. *Optics Communications* 111.5–6 (Oct. 1994),
13 pp. 536–547. DOI: 10.1016/0030-4018(94)90533-9 (cit. on p. 14).
- 14 [30] Silvia Aldaz, Luis M. Escudero, and Matthew Freeman. “Live Imaging of
15 Drosophila Imaginal Disc Development”. *Proceedings of the National Academy of
16 Sciences* 107.32 (Aug. 2010), pp. 14217–14222. DOI: 10.1073/pnas.1008623107
17 (cit. on p. 14).
- 18 [31] Jean-Léon Maître et al. “Asymmetric division of contractile domains couples cell
19 positioning and fate specification”. *Nature* 536.7616 (Aug. 2016), pp. 344–348.
20 DOI: 10.1038/nature18958 (cit. on pp. 14, 22).
- 21 [32] Emmanuel G. Reynaud, Uroš Kržič, Klaus Greger, and Ernst H.K. Stelzer. “Light
22 sheet-based fluorescence microscopy: more dimensions, more photons, and less
23 photodamage”. *HFSP Journal* 2.5 (Oct. 2008), pp. 266–275. DOI: 10.2976/1.
24 2974980 (cit. on p. 14).
- 25 [33] Stelzer. “Contrast, resolution, pixelation, dynamic range and signal-to-noise ratio:
26 fundamental limits to resolution in fluorescence light microscopy”. *Journal
27 of Microscopy* 189.1 (Jan. 1998). This is also the reason why it is sufficient to
28 store the square root of the count rate. That number will contain all the available
29 information., pp. 15–24. DOI: 10.1046/j.1365-2818.1998.00290.x (cit. on
30 p. 14).
- 31 [34] H. Siedentopf and R. Zsigmondy. “Über Sichtbarmachung und Größenbestimmung
32 ultramikroskopischer Teilchen, mit besonderer Anwendung auf Goldrubiingläser”.
33 *Annalen der Physik* 315.1 (1902), pp. 1–39. DOI: 10.1002/andp.19023150102
34 (cit. on p. 15).

References cited in the thesis

- [35] A H Voie, D H Burns, and F A Spelman. “Orthogonal-plane fluorescence optical sectioning: three-dimensional imaging of macroscopic biological specimens”. *Journal of Microscopy* 170.Pt 3 (June 1993), pp. 229–36. DOI: 8371260 (cit. on p. 15).
- [36] Arne H. Voie and Francis A. Spelman. “Three-dimensional reconstruction of the cochlea from two-dimensional images of optical sections”. *Computerized Medical Imaging and Graphics* 19.5 (Sept. 1995), pp. 377–384. DOI: 10.1016/0895-6111(95)00034-8 (cit. on p. 15).
- [37] Eran Fuchs, Jules S. Jaffe, Richard A. Long, and Farooq Azam. “Thin laser light sheet microscope for microbial oceanography”. *Optics Express* 10.2 (Jan. 2002), pp. 145–154. DOI: 10.1364/OE.10.000145 (cit. on p. 15).
- [38] Jan Huisken, Jim Swoger, Filippo Del Bene, Joachim Wittbrodt, and Ernst H. K Stelzer. “Optical Sectioning Deep Inside Live Embryos by Selective Plane Illumination Microscopy”. *Science* 305.5686 (2004), pp. 1007–1009 (cit. on pp. 16, 17).
- [39] Jérémie Capoulade, Malte Wachsmuth, Lars Hufnagel, and Michael Knop. “Quantitative fluorescence imaging of protein diffusion and interaction in living cells”. *Nature Biotechnology* 29.9 (Sept. 2011), pp. 835–839. DOI: 10.1038/nbt.1928 (cit. on p. 16).
- [40] Yicong Wu et al. “Inverted selective plane illumination microscopy (iSPIM) enables coupled cell identity lineaging and neurodevelopmental imaging in *Caenorhabditis elegans*”. *Proceedings of the National Academy of Sciences* 108.43 (Oct. 2011). iSPIM, tracking c. elegnas nuclei, pp. 17708–17713. DOI: 10.1073/pnas.1108494108 (cit. on p. 16).
- [41] Abhishek Kumar et al. “Dual-view plane illumination microscopy for rapid and spatially isotropic imaging”. *Nature Protocols* 9.11 (Nov. 2014). diSPIM, pp. 2555–2573. DOI: 10.1038/nprot.2014.172 (cit. on pp. 16, 17).
- [42] Jan Huisken and Didier Y. R. Stainier. “Even fluorescence excitation by multidirectional selective plane illumination microscopy (mSPIM)”. *Optics Letters* 32.17 (2007), pp. 2608–2610. DOI: 10.1364/OL.32.002608 (cit. on pp. 16, 17, 21).
- [43] Benjamin Schmid et al. “High-speed panoramic light-sheet microscopy reveals global endodermal cell dynamics”. *Nature Communications* 4 (July 2013). zebrafish sphere projection + FEP tube. DOI: 10.1038/ncomms3207 (cit. on pp. 16, 17).

- 1 [44] Raghav K. Chhetri et al. “Whole-animal functional and developmental imaging
2 with isotropic spatial resolution”. *Nature Methods* 12.12 (Dec. 2015), pp. 1171–
3 1178. DOI: [10.1038/nmeth.3632](https://doi.org/10.1038/nmeth.3632) (cit. on pp. 16, 17, 37).
- 4 [45] Jan Huisken and Didier Y. R. Stainier. “Selective plane illumination microscopy
5 techniques in developmental biology”. *Development* 136.12 (June 2009), pp. 1963–
6 1975. DOI: [10.1242/dev.022426](https://doi.org/10.1242/dev.022426) (cit. on p. 16).
- 7 [46] Philipp J. Keller, Annette D. Schmidt, Joachim Wittbrodt, and Ernst H. K.
8 Stelzer. “Reconstruction of Zebrafish Early Embryonic Development by Scanned
9 Light Sheet Microscopy”. *Science* 322.5904 (Nov. 2008), pp. 1065–1069. DOI: [10.1126/science.1162493](https://doi.org/10.1126/science.1162493) (cit. on pp. 16, 17, 21).
- 11 [47] Takehiko Ichikawa et al. “Live Imaging of Whole Mouse Embryos during Gas-
12 trulation: Migration Analyses of Epiblast and Mesodermal Cells”. *PLoS ONE* 8.7
13 (July 2013). post implantation, e64506. DOI: [10.1371/journal.pone.0064506](https://doi.org/10.1371/journal.pone.0064506)
14 (cit. on pp. 16, 25, 26).
- 15 [48] Ryan S. Udan, Victor G. Piazza, Chih-wei Hsu, Anna-Katerina Hadjantonakis,
16 and Mary E. Dickinson. “Quantitative imaging of cell dynamics in mouse em-
17 bryos using light-sheet microscopy”. *Development* (Oct. 2014). post implantation,
18 dev.111021. DOI: [10.1242/dev.111021](https://doi.org/10.1242/dev.111021) (cit. on pp. 16, 25).
- 19 [49] Francesca Cella Zanacchi et al. “Live-cell 3D super-resolution imaging in thick
20 biological samples”. *Nature Methods* 8.12 (Dec. 2011), pp. 1047–1049. DOI: [10.1038/nmeth.1744](https://doi.org/10.1038/nmeth.1744) (cit. on p. 17).
- 22 [50] Mike Friedrich, Qiang Gan, Vladimir Ermolayev, and Gregory S. Harms. “STED-
23 SPIM: Stimulated Emission Depletion Improves Sheet Illumination Microscopy
24 Resolution”. *Biophysical Journal* 100.8 (Apr. 2011), pp. L43–L45. DOI: [10.1016/j.bpj.2010.12.3748](https://doi.org/10.1016/j.bpj.2010.12.3748) (cit. on p. 17).
- 26 [51] Philipp J. Keller et al. “Fast, high-contrast imaging of animal development with
27 scanned light sheet-based structured-illumination microscopy”. *Nature Methods*
28 7.8 (Aug. 2010). light-sheet structured illumination, pp. 637–642. DOI: [10.1038/nmeth.1476](https://doi.org/10.1038/nmeth.1476) (cit. on p. 17).
- 30 [52] Bo-Jui Chang, Victor Didier Perez Meza, and Ernst H. K. Stelzer. “csiLSFM
31 combines light-sheet fluorescence microscopy and coherent structured illumination
32 for a lateral resolution below 100 nm”. *Proceedings of the National Academy of
33 Sciences* 114.19 (May 2017), pp. 4869–4874. DOI: [10.1073/pnas.1609278114](https://doi.org/10.1073/pnas.1609278114)
34 (cit. on p. 17).

References cited in the thesis

- [53] K. Greger, J. Swoger, and E. H. K. Stelzer. “Basic building units and properties of a fluorescence single plane illumination microscope”. *Review of Scientific Instruments* 78.2 (Feb. 2007), pp. 023705–023705–7. DOI: doi:10.1063/1.2428277 (cit. on p. 18).
- [54] Bahaa E. A. Saleh and Malvin Carl Teich. *Fundamentals of Photonics*. John Wiley & Sons, Mar. 2007 (cit. on p. 19).
- [55] Carl Costanzi and John R. Pehrson. “Histone macroH2A1 is concentrated in the inactive X chromosome of female mammals”. *Nature* 393.6685 (June 1998), pp. 599–601. DOI: 10.1038/31275 (cit. on p. 22).
- [56] Frédérique Bard et al. “Peripherally administered antibodies against amyloid - peptide enter the central nervous system and reduce pathology in a mouse model of Alzheimer disease”. *Nature Medicine* 6.8 (Aug. 2000), pp. 916–919. DOI: 10.1038/78682 (cit. on p. 22).
- [57] Jennifer Nichols et al. “Formation of Pluripotent Stem Cells in the Mammalian Embryo Depends on the POU Transcription Factor Oct4”. *Cell* 95.3 (Oct. 1998), pp. 379–391. DOI: 10.1016/S0092-8674(00)81769-9 (cit. on p. 22).
- [58] Ariel A. Avilion et al. “Multipotent cell lineages in early mouse development depend on SOX2 function”. *Genes & Development* 17.1 (Jan. 2003), pp. 126–140. DOI: 10.1101/gad.224503 (cit. on p. 22).
- [59] Ralph Gräf, Jens Rietdorf, and Timo Zimmermann. “Live Cell Spinning Disk Microscopy”. *Microscopy Techniques. Advances in Biochemical Engineering*. DOI: 10.1007/b102210. Springer, Berlin, Heidelberg, 2005, pp. 57–75 (cit. on p. 22).
- [60] G. S. Kino. “Intermediate Optics in Nipkow Disk Microscopes”. *Handbook of Biological Confocal Microscopy*. DOI: 10.1007/978-1-4615-7133-9_10. Springer, Boston, MA, 1990, pp. 105–111 (cit. on p. 22).
- [61] Akihiko Nakano. “Spinning-disk Confocal Microscopy — A Cutting-Edge Tool for Imaging of Membrane Traffic”. *Cell Structure and Function* 27.5 (2002), pp. 349–355. DOI: 10.1247/csf.27.349 (cit. on p. 22).
- [62] Ekaterina Korotkevich et al. “The Apical Domain Is Required and Sufficient for the First Lineage Segregation in the Mouse Embryo”. *Developmental Cell* 40.3 (2017), 235–247.e7. DOI: http://dx.doi.org/10.1016/j.devcel.2017.01.006 (cit. on p. 22).
- [63] Jean-Léon Maître, Ritsuya Niwayama, Hervé Turlier, François Nédélec, and Takashi Hiiragi. “Pulsatile cell-autonomous contractility drives compaction in the mouse embryo”. *Nature Cell Biology* 17.7 (July 2015), pp. 849–855. DOI: 10.1038/ncb3185 (cit. on p. 22).

- 1 [64] Jens-Erik Dietrich et al. “Venus trap in the mouse embryo reveals distinct molec-
2 uar dynamics underlying specification of first embryonic lineages”. *EMBO reports*
3 16.8 (Aug. 2015), pp. 1005–1021. DOI: 10.15252/embr.201540162 (cit. on p. 22).
- 4 [65] Sonja Nowotschin, Anna Ferrer-Vaquer, and Anna-Katerina Hadjantonakis.
5 “Chapter 20 - Imaging Mouse Development with Confocal Time-Lapse Mi-
6 croscopy”. *Methods in Enzymology*. Ed. by Paul M. Wasserman and Philippe M.
7 Soriano. Vol. 476. Guide to Techniques in Mouse Development, Part A: Mice,
8 Embryos, and Cells, 2nd Edition. Academic Press, 2010, pp. 351–377 (cit. on
9 p. 23).
- 10 [66] Lewis Wolpert. *Principles of Development*. OUP Oxford, Jan. 2011 (cit. on p. 23).
- 11 [67] Adam S. Doherty and Richard M. Schultz. “Culture of Preimplantation Mouse
12 Embryos”. *Developmental Biology Protocols*. Methods in Molecular Biology™.
13 DOI: 10.1385/1-59259-685-1:47. Humana Press, 2000, pp. 47–52 (cit. on p. 23).
- 14 [68] Jens-Erik Dietrich and Takashi Hiiragi. “Stochastic patterning in the mouse pre-
15 implantation embryo”. *Development* 134.23 (Dec. 2007), pp. 4219–4231. DOI: 10.
1242/dev.003798 (cit. on p. 23).
- 17 [69] W. Denk, J. H. Strickler, and W. W. Webb. “Two-photon laser scanning fluo-
18 rescence microscopy”. *Science* 248.4951 (Apr. 1990), pp. 73–76. DOI: 10.1126/
19 science.2321027 (cit. on p. 23).
- 20 [70] Jayne M. Squirrell, David L. Wokosin, John G. White, and Barry D. Bavis-
21 ter. “Long-term two-photon fluorescence imaging of mammalian embryos with-
22 out compromising viability”. *Nature Biotechnology* 17.8 (Aug. 1999). low dam-
23 age live-cell imaging with two-photon caser scanning hamster, pp. 763–767. DOI:
24 10.1038/11698 (cit. on p. 23).
- 25 [71] Katie McDole, Yuan Xiong, Pablo A. Iglesias, and Yixian Zheng. “Lineage map-
26 ping the pre-implantation mouse embryo by two-photon microscopy, new in-
27 sights into the segregation of cell fates”. *Developmental Biology* 355.2 (July 2011),
28 pp. 239–249. DOI: 10.1016/j.ydbio.2011.04.024 (cit. on p. 23).
- 29 [72] Kazuo Yamagata, Rinako Suetsugu, and Teruhiko Wakayama. “Long-Term, Six-
30 Dimensional Live-Cell Imaging for the Mouse Preimplantation Embryo That Does
31 Not Affect Full-Term Development”. *Journal of Reproduction and Development*
32 55.3 (2009), pp. 343–350. DOI: 10.1262/jrd.20166 (cit. on p. 23).
- 33 [73] Gustavo de Medeiros et al. “Confocal multiview light-sheet microscopy”. *Nature
34 Communications* 6 (Nov. 2015), p. 8881. DOI: 10.1038/ncomms9881 (cit. on pp. 25,
35 26).

References cited in the thesis

- [74] Laura Panavaite et al. “3D-geec: a method for studying mouse peri-implantation development”. *Mechanisms of Development*. 18th International Congress of Developmental Biology 18-22 June, University Cultural Centre, National University of Singapore 145. Supplement (July 2017), S78–S79. DOI: 10.1016/j.mod.2017.04.189 (cit. on p. 25).
- [75] Yu-Chih Hsu. “In vitro development of individually cultured whole mouse embryos from blastocyst to early somite stage”. *Developmental Biology* 68.2 (Feb. 1979). post-implantation culture, pp. 453–461. DOI: 10.1016/0012-1606(79)90217-3 (cit. on p. 25).
- [76] Fu-Jen Huang, Tsung-Chieh J. Wu, and Meng-Yin Tsai. “Effect of retinoic acid on implantation and post-implantation development of mouse embryos in vitro”. *Human Reproduction* 16.10 (Oct. 2001). post-implantation culture, pp. 2171–2176. DOI: 10.1093/humrep/16.10.2171 (cit. on p. 25).
- [77] Sonja Nowotschin and Anna-Katerina Hadjantonakis. “Cellular dynamics in the early mouse embryo: from axis formation to gastrulation”. *Current Opinion in Genetics & Development*. Developmental mechanisms, patterning and evolution 20.4 (Aug. 2010), pp. 420–427. DOI: 10.1016/j.gde.2010.05.008 (cit. on p. 25).
- [78] Monica D. Garcia, Ryan S. Udan, Anna-Katerina Hadjantonakis, and Mary E. Dickinson. “Live Imaging of Mouse Embryos”. *Cold Spring Harbor Protocols* 2011.4 (Apr. 2011), pdb.top104. DOI: 10.1101/pdb.top104 (cit. on p. 25).
- [79] Alessandro Bria and Giulio Iannello. “TeraStitcher - A tool for fast automatic 3D-stitching of teravoxel-sized microscopy images”. *BMC Bioinformatics* 13 (Nov. 2012), p. 316. DOI: 10.1186/1471-2105-13-316 (cit. on p. 26).
- [80] Gergely Katona et al. “Fast two-photon in vivo imaging with three-dimensional random-access scanning in large tissue volumes”. *Nature Methods* 9.2 (Feb. 2012), pp. 201–208. DOI: 10.1038/nmeth.1851 (cit. on p. 27).
- [81] Hiroshi Hama et al. “Scale: a chemical approach for fluorescence imaging and reconstruction of transparent mouse brain”. *Nature Neuroscience* 14.11 (Nov. 2011), pp. 1481–1488. DOI: 10.1038/nn.2928 (cit. on p. 27).
- [82] Ali Ertürk et al. “Three-dimensional imaging of solvent-cleared organs using 3DISCO”. *Nature Protocols* 7.11 (Nov. 2012), pp. 1983–1995. DOI: 10.1038/nprot.2012.119 (cit. on p. 27).
- [83] Ali Ertürk et al. “Three-dimensional imaging of the unsectioned adult spinal cord to assess axon regeneration and glial responses after injury”. *Nature Medicine* 18.1 (Jan. 2012), pp. 166–171. DOI: 10.1038/nm.2600 (cit. on p. 27).

- 1 [84] Takaaki Kuwajima et al. “ClearT: a detergent- and solvent-free clearing method
2 for neuronal and non-neuronal tissue”. *Development* 140.6 (Mar. 2013), pp. 1364–
3 1368. DOI: [10.1242/dev.091844](https://doi.org/10.1242/dev.091844) (cit. on p. 27).
- 4 [85] Meng-Tsen Ke, Satoshi Fujimoto, and Takeshi Imai. “SeeDB: a simple and
5 morphology-preserving optical clearing agent for neuronal circuit reconstruction”.
6 *Nature Neuroscience* 16.8 (Aug. 2013), pp. 1154–1161. DOI: [10.1038/nn.3447](https://doi.org/10.1038/nn.3447)
7 (cit. on p. 27).
- 8 [86] Kwanghun Chung and Karl Deisseroth. “CLARITY for mapping the nervous sys-
9 tem”. *Nature Methods* 10.6 (June 2013), pp. 508–513. DOI: [10.1038/nmeth.2481](https://doi.org/10.1038/nmeth.2481)
10 (cit. on p. 27).
- 11 [87] Raju Tomer, Li Ye, Brian Hsueh, and Karl Deisseroth. “Advanced CLARITY for
12 rapid and high-resolution imaging of intact tissues”. *Nature Protocols* 9.7 (July
13 2014), pp. 1682–1697. DOI: [10.1038/nprot.2014.123](https://doi.org/10.1038/nprot.2014.123) (cit. on p. 27).
- 14 [88] Etsuo A. Susaki et al. “Whole-Brain Imaging with Single-Cell Resolution Us-
15 ing Chemical Cocktails and Computational Analysis”. *Cell* 157.3 (Apr. 2014),
16 pp. 726–739. DOI: [10.1016/j.cell.2014.03.042](https://doi.org/10.1016/j.cell.2014.03.042) (cit. on p. 27).
- 17 [89] Nicolas Renier et al. “iDISCO: A Simple, Rapid Method to Immunolabel Large
18 Tissue Samples for Volume Imaging”. *Cell* 159.4 (Nov. 2014), pp. 896–910. DOI:
19 [10.1016/j.cell.2014.10.010](https://doi.org/10.1016/j.cell.2014.10.010) (cit. on p. 27).
- 20 [90] Kazuki Tainaka et al. “Whole-Body Imaging with Single-Cell Resolution by Tissue
21 Decolorization”. *Cell* 159.4 (Nov. 2014), pp. 911–924. DOI: [10.1016/j.cell.2014.10.034](https://doi.org/10.1016/j.cell.2014.10.034) (cit. on p. 28).
- 22 [91] Tongcang Li et al. “Axial Plane Optical Microscopy”. *Scientific Reports* 4 (Dec.
23 2014). DOI: [10.1038/srep07253](https://doi.org/10.1038/srep07253) (cit. on p. 28).
- 24 [92] Matthew B. Bouchard et al. “Swept confocally-aligned planar excitation (SCAPE)
25 microscopy for high-speed volumetric imaging of behaving organisms”. *Nature
26 Photonics* 9.2 (Feb. 2015), pp. 113–119. DOI: [10.1038/nphoton.2014.323](https://doi.org/10.1038/nphoton.2014.323) (cit.
27 on p. 28).
- 28 [93] Gerald Donnert, Christian Eggeling, and Stefan W. Hell. “Major signal increase in
29 fluorescence microscopy through dark-state relaxation”. *Nature Methods* 4.1 (Jan.
30 2007). peak intensity more important than average, pp. 81–86. DOI: [10.1038/nmeth986](https://doi.org/10.1038/nmeth986) (cit. on p. 29).
- 31 [94] Na Ji, Jeffrey C. Magee, and Eric Betzig. “High-speed, low-photodamage nonlin-
32 ear imaging using passive pulse splitters”. *Nature Methods* 5.2 (Feb. 2008). TPE,
33 pulse splitter, peak intensity more important than average, pp. 197–202. DOI:
34 [10.1038/nmeth.1175](https://doi.org/10.1038/nmeth.1175) (cit. on p. 29).

References cited in the thesis

- [95] Sarah Frisken Gibson and Frederick Lanni. “Experimental test of an analytical model of aberration in an oil-immersion objective lens used in three-dimensional light microscopy”. *JOSA A* 9.1 (Jan. 1992), pp. 154–166. DOI: 10.1364/JOSAA.9.000154 (cit. on p. 39).
- [96] Jizhou Li, Feng Xue, and Thierry Blu. “Fast and accurate three-dimensional point spread function computation for fluorescence microscopy”. *JOSA A* 34.6 (June 2017), pp. 1029–1034. DOI: 10.1364/JOSAA.34.001029 (cit. on p. 39).
- [97] Uroš Kržič. “Multiple-view microscopy with light-sheet based fluorescence microscope”. PhD thesis. Germany: Ruperto-Carola University of Heidelberg, 2009 (cit. on p. 42).
- [98] M. Temerinac-Ott et al. “Multiview Deblurring for 3-D Images from Light-Sheet-Based Fluorescence Microscopy”. *IEEE Transactions on Image Processing* 21.4 (Apr. 2012), pp. 1863–1873. DOI: 10.1109/TIP.2011.2181528 (cit. on p. 42).
- [99] M. Temerinac-Ott, O. Ronneberger, R. Nitschke, W. Driever, and H. Burkhardt. “Spatially-variant Lucy-Richardson deconvolution for multiview fusion of microscopical 3D images”. *2011 IEEE International Symposium on Biomedical Imaging: From Nano to Macro*. Mar. 2011, pp. 899–904. DOI: 10.1109/ISBI.2011.5872549 (cit. on p. 42).
- [100] Khalid Sayood. *Introduction to Data Compression, Fourth Edition*. 4th ed. The Morgan Kaufmann Series in Multimedia Information and Systems. Morgan Kaufmann, 2012 (cit. on p. 42).
- [101] Claude E. Shannon. “A mathematical theory of communication”. *The Bell System Technical Journal* 27.4 (Oct. 1948), pp. 623–656. DOI: 10.1002/j.1538-7305.1948.tb00917.x (cit. on p. 43).
- [102] Claude E. Shannon. “A mathematical theory of communication”. *The Bell System Technical Journal* 27.3 (July 1948), pp. 379–423. DOI: 10.1002/j.1538-7305.1948.tb01338.x (cit. on p. 43).
- [103] David A. Huffman. “A Method for the Construction of Minimum-Redundancy Codes”. *Proceedings of the IRE* 40.9 (Sept. 1952), pp. 1098–1101. DOI: 10.1109/JRPROC.1952.273898 (cit. on p. 43).
- [104] N. Ahmed, T. Natarajan, and K. R. Rao. “Discrete Cosine Transform”. *IEEE Transactions on Computers* C-23.1 (Jan. 1974), pp. 90–93. DOI: 10.1109/TC.1974.223784 (cit. on p. 48).
- [105] Stephane G. Mallat. “A theory for multiresolution signal decomposition : the wavelet representation”. *IEEE Transaction on Pattern Analysis and Machine Intelligence* (1989) (cit. on p. 50).

-
- 1 [106] William B. Pennebaker and Joan L. Mitchell. *JPEG: Still Image Data Compre-*
- 2 sion Standard. Springer Science & Business Media, Dec. 1992 (cit. on p. 51).
- 3 [107] M.J. Weinberger, G. Seroussi, and G. Sapiro. “The LOCO-I lossless image com-
- 4 pression algorithm: principles and standardization into JPEG-LS”. *IEEE Trans-*
- 5 *actions on Image Processing* 9.8 (Aug. 2000), pp. 1309–1324. DOI: 10.1109/83.
- 6 855427 (cit. on p. 51).
- 7 [108] Jeremy C. Simpson et al. “Genome-wide RNAi screening identifies human proteins
- 8 with a regulatory function in the early secretory pathway”. *Nature Cell Biology*
- 9 14.7 (July 2012), pp. 764–774. DOI: 10.1038/ncb2510 (cit. on p. 56).